

Article

Variable Dimensional Scaling Method: A Novel Method for Path Planning and Inverse Kinematics

Longfei Jia ^{1,2} , Zhiyuan Yu ^{1,2}, Haiping Zhou ^{1,2}, Zhe Pan ¹, Yangsheng Ou ³, Yaxing Guo ¹ and Yuping Huang ^{1,2,*} 

¹ Beijing Institute of Precision Mechatronics and Controls, Beijing 100076, China

² Laboratory of Aerospace Servo Actuation and Transmission, Beijing 100076, China

³ China Academy of Aerospace Science and Innovation, Beijing 100076, China

* Correspondence: huangyp@2008.sina.com

Abstract: Traditional methods for solving the inverse kinematics of a hyper-redundant manipulator (HRM) can only plan the path of the end-effector with a complicated solving process, where obstacle avoidance is also not considered. To solve the above problems, a novel method for solving inverse kinematics of HRM is proposed in this paper: the variable dimension scaling method (VDSM), which can solve complex inverse kinematics while avoiding obstacles. Through this method, the path of the end-effector is scaled under a certain proportion and is adjusted depending on the position of the obstacle, which has good universality. The number of link angles changed is as small as possible in the process of achieving the end-effector moving along the desired path. With the redundancy of HRM, obstacle avoidance can be implemented in any environment by the proposed method. Through simulation and experiments in different environments, the above advantages of VDSM are verified.

Keywords: variable dimension scaling method; path planning; inverse kinematics; obstacle avoidance; hyper-redundant manipulator



Citation: Jia, L.; Yu, Z.; Zhou, H.; Pan, Z.; Ou, Y.; Guo, Y.; Huang, Y. Variable Dimensional Scaling Method: A Novel Method for Path Planning and Inverse Kinematics. *Machines* **2022**, *10*, 1030. <https://doi.org/10.3390/machines10111030>

Academic Editors: Jonathan Crespo and Ramon Barber

Received: 10 October 2022

Accepted: 1 November 2022

Published: 4 November 2022

Publisher's Note: MDPI stays neutral with regard to jurisdictional claims in published maps and institutional affiliations.



Copyright: © 2022 by the authors. Licensee MDPI, Basel, Switzerland. This article is an open access article distributed under the terms and conditions of the Creative Commons Attribution (CC BY) license (<https://creativecommons.org/licenses/by/4.0/>).

1. Introduction

It is necessary to replace human with manipulator under some hazardous circumstances, such as object carrying, surgery, rescue, non-conventional machining, nuclear power plant monitoring, etc. Hyper-redundant manipulators (HRMs) have multiple degrees of freedom and motion modes, and ability for multi-objective optimization, which can achieve excellent environmental adaptability and extremely high obstacle-avoidance ability to perform tasks in small, complex, and unstructured environments. In actual applications, path planning and the solution of inverse kinematics are necessary to complete the movement and control of the manipulator. Therefore, some methods of solving inverse kinematics have been put forward that can be classified into three categories: geometric methods, numerical methods, and intelligent algorithms.

The process of solving the inverse kinematics of HRMs can be converted into an optimization problem by applying numerical methods, and the problem can be solved iteratively as the objective function is determined. There are some methods commonly used in numerical methods, including the Jacobian pseudo-inverse method [1], damped least-squares method [2,3], and gradient-projection method [4,5], which can be used to calculate the joint angle in real time according to the position of end-effector. For numerical methods, there are no restrictions on the configurations and geometric parameters of the HRM, allowing a universal solution framework for all kinds of manipulators to be constructed, and the calculation process is more flexible. However, real-time performance and high precision cannot be achieved simultaneously in numerical methods, and the setting of the initial point also affects the convergence of numerical methods. Due to the existence of numerous iterations, the solving speed of the numerical method is generally much slower

than that of the geometric method under the same accuracy requirements, and the existence of cumulative errors will also affect the control accuracy.

With the development of intelligence, more and more intelligent optimization algorithms have been proposed to resolve the inverse kinematics of the HRM, such as neural network algorithms [6–8], particle swarm optimization algorithms [9,10], differential evolution algorithms [11,12], genetic algorithms [13], simulated anneal arithmetic [14], firefly swarm algorithms [15–17], artificial bee swarm algorithms [18], and other intelligent algorithms. Although intelligent algorithms can achieve an optimized solution, multiple iterations are carried out, resulting in a longer calculation time with a loss of the capability for real-time solving and a possibility of falling into the local optimal point or non-convergence, while the ability to avoid obstacles is not considered in many intelligent algorithms.

The process of solving inverse kinematics by using numerical methods [19,20] and intelligent algorithms is often more complicated; thus, geometric methods have been introduced to simplify the process, reducing the difficulty of solving. As the earliest applied methods for solving the inverse kinematics of HRM, these methods only simplify the concrete structure of HRM, establish constraint equations between the link and the position of the end-effector by geometric relationship, and then solve the angle of the joint by the end-effector position. The process of geometric methods can be generally divided into three steps: (1) Determine the configuration of the HRM, (2) solve the coordinates of each key point, and (3) solve the angle of each joint. The computational speed, efficiency, and accuracy of geometric methods are better than those of numerical methods requiring an iterative solution, and the computational complexity is lower than that of numerical methods and intelligent algorithms, which is convenient for achieving the real-time control of the HRM. Geometric methods possess the advantages of great geometrical intuitiveness and low computation cost, and can be divided into several types: repeated path method [21–23], ridge method [24], segmented geometry method, equally effective method, parameterization method, etc.

Xie [22] proposed a repeated path method for a rigid snake manipulator, which has high positioning accuracy and a short computation time. The repeated path method can be utilized to solve the inverse kinematics of snake robots, cable drive manipulators, continuous manipulators, and flexible manipulators. However, the inverse solution is unique and certain, and the curvature of the path cannot be too large, which limits the motion space of the manipulator and reduces the flexibility and redundancy of the HRM. Jia [23] proposed the MDA + RRT algorithm for path planning on the basis of the RRT algorithm, and theoretically analyzed the relationship between four parameters, i.e., the length of the link, the maximum joint angle, the step of the path, and the maximum angle between two adjacent lines in the path, so as to solve the problem of the limitation of the deviation angle of a joint in the HRM.

The traditional ridge line method fits all key points to the ridge line, reducing the redundancy of HRMs. Zhang [24] designed the expression of the spiral curve based on the ridge method and proposed a shape-fitting algorithm to constrain the macroscopic shape of snake robots and calculate the angle of each joint in the process of motion by using the phase-shifting and angle-solving algorithm. The ridge line method is mostly used for snake robots, quasi-continuous manipulators, or continuous manipulators, especially for HRMs with degrees of freedom greater than 20. The application of the ridge line method to HRM can greatly reduce the difficulty of solving inverse kinematics, but the redundancy of HRM will also be greatly reduced.

The geometric methods mentioned above can hardly meet the constraints of obstacle avoidance and cannot take advantage of the redundancy of HRM. With the help of Robotics Toolbox and ROS, only the end trajectory can be planned while leaving other problems unsolved, and the inverse kinematics can not be solved under a circumstance where there are too many degrees of freedom. Alejandro [25] proposed a novel variant of differential evolution for variable-length vector optimization named VLV-DE, which worked well for mobile robots, but was not suitable for redundant manipulators. The research for the

corresponding path planning and inverse kinematics of the snake manipulator (quasi-continuous manipulator) still focuses on follow-the-leader (also known as path-following planning, tip following, and snake motion) repeated path planning. The end-effector and each joint move along a path planned by these methods in repetition, which limits the redundancy of HRM, and the results of inverse kinematics solutions are undesired.

The traditional method for solving the inverse kinematics of HRM cannot control the motion path of the intermediate joint, or, at most, one or two joints. The solving process is complicated, and obstacle avoidance cannot be taken into account in the solving process. In this paper, a novel path planning and inverse kinematics solution method, “varied dimensional scaling method (VDSM)”, is proposed. The method scales the path of the end-effector under a certain proportion and adjusts the path of the end-effector and each joint according to the specific position of the obstacle, which is in possession of good versatility.

The VDSM introduced in this paper inherits the advantages of the traditional geometric method:

- Solvable. Problems can be solved when the inverse kinematics of the HRM is difficult to solve and the solution is not unique;
- Real-time. Compared with numerical methods and intelligent algorithms, fast calculation speed and low computational complexity are achieved, which are convenient for the realization of real-time control;
- Intuitive. Good geometric intuition is exhibited.

Compared with traditional methods and other methods, the VDSM has the following characteristics:

- Obstacle avoidance. This method makes full use of the redundancy performance of HRMs to achieve obstacle avoidance;
- Variability of dimension. This method converts 3D paths into 2D paths. After the 2D paths of the end and each joint are planned, these are then converted into 3D paths to solve the inverse motion and acquire the change rule of the angle of each joint;
- Constant ratio. According to the length of each link, the scaling relationship can be developed by this method to carry out path planning and solution of inverse kinematics;
- Efficiency. This method can change the fewest degrees of freedom to realize the motion of the end-effector on the desired path;
- Simplification. This method converts the 3D obstacle avoidance into a 2D obstacle avoidance and simplifies the solving process of inverse kinematics while retaining the redundancy of the manipulator;
- Non-iterative. This method requires no iterative solving during the solving process of inverse kinematics, and the inverse kinematics solution can be obtained at one time;
- Generality. This method is appropriate for all kinds of obstacle environments.

The layout of this paper is as follows. In Section 2, the manipulator is modeled and the transformation relationship between the joint angle and link angle is derived. Section 3 describes the principle of VDSM where no obstacle exists. Section 4 introduces the principle of VDSM when there are obstacles, including three obstacle environments. Section 5 presents the transformation relationship between various motion parameters. Section 6 verifies the effectiveness of the VDSM through simulation under three kinds of obstacle models. In Section 7, the effectiveness of the VDSM is checked by experiments. Section 8 presents the conclusion.

2. Modeling

The model of the cable-driven HRM and Denavit–Hartenberg (D-H) coordinate system are shown in Figure 1. The entirety of the manipulator possesses a translational freedom X_0 in one direction along with the propulsion platform. The manipulator is composed of eight serial links with a total of 16 rotational degrees of freedom, and each link has two degrees of freedom: pitch angle θ_i and yaw angle α_i . Each link is driven by three cables, and the

position of each cable is driven by each motor. In total, 24 cables are driven by 24 motors, controlling 16 rotational degrees of freedom of the eight links.

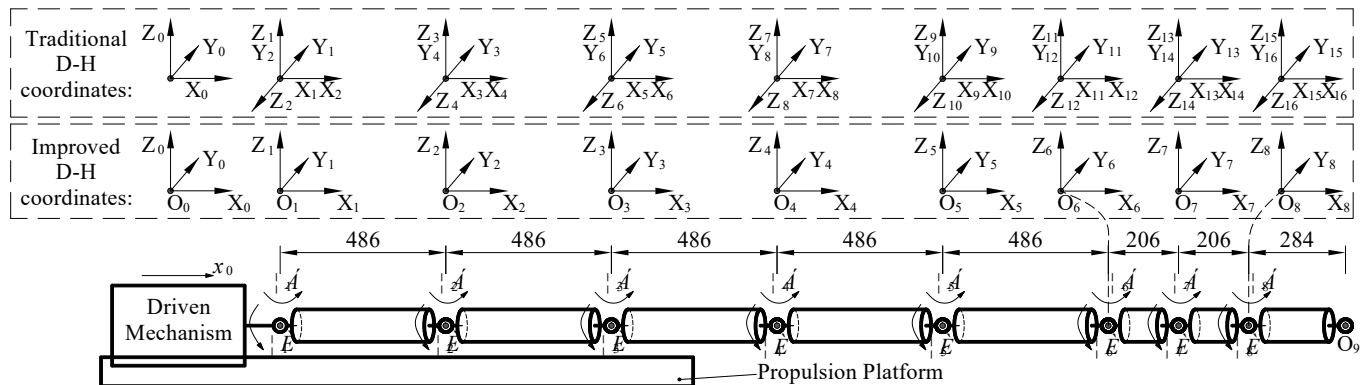


Figure 1. Simplified model and D-H coordinate system of an HRM.

In order to analyze and solve the kinematics of the cable-driven HRM, the corresponding D-H coordinate system should be established. However, as a general solution method, the D-H method is not unified in its standards, which are often established with different rules and habits. In the traditional D-H coordinate system, the coordinate system shown in the first line of Figure 1 is used to establish the D-H coordinate system with 16 degrees of freedom, and the parameters of the D-H coordinate system in 16 lines need to be listed. In order to facilitate the calculation of the forward and inverse kinematics, 16 coordinate systems are simplified into 8 coordinate systems, as shown in the middle row in Figure 1 in this paper, which are presented in Table 1. The transformation matrix between the two coordinate systems can be obtained by making the coordinate $\{O_{i-1}\}$ translate a_i along the X_{i-1} axis, rotating α_i of Z_{i-1} , then rotating θ_i to coordinate $\{O_i\}$, and finally translating d_i along Z_i axis, as shown in Equation (1).

$$\begin{aligned}
 {}_i^{i-1}T &= \text{Trans}(a_i, 0, 0) \cdot \text{Rot}(z_{i-1}, \alpha_i) \cdot \text{Rot}(y_i, \theta_i) \cdot \text{Trans}(0, 0, d_i) \\
 &= \begin{bmatrix} 1 & 0 & 0 & a_i \\ 0 & 1 & 0 & 0 \\ 0 & 0 & 1 & 0 \\ 0 & 0 & 0 & 1 \end{bmatrix} \cdot \begin{bmatrix} c\alpha_i & -s\alpha_i & 0 & 0 \\ s\alpha_i & c\alpha_i & 0 & 0 \\ 0 & 0 & 1 & 0 \\ 0 & 0 & 0 & 1 \end{bmatrix} \cdot \begin{bmatrix} c\theta_i & 0 & s\theta_i & 0 \\ 0 & 1 & 0 & 0 \\ -s\theta_i & 0 & c\theta_i & 0 \\ 0 & 0 & 0 & 1 \end{bmatrix} \\
 &= \begin{bmatrix} c\alpha_i \cdot c\alpha_i & -s\alpha_i & c\alpha_i \cdot s\alpha_i & a_i \\ s\alpha_i \cdot c\alpha_i & c\alpha_i & s\alpha_i \cdot s\alpha_i & 0 \\ -s\alpha_i & 0 & c\alpha_i & 0 \\ 0 & 0 & 0 & 1 \end{bmatrix}, \quad (1) \\
 &= \begin{bmatrix} {}_i^{i-1}T & {}_i^{i-1}T \\ \mathbf{0}^T & 1 \end{bmatrix}
 \end{aligned}$$

where c stands for \cos and s stands for \sin , and these abbreviations are adopted hereafter. ${}_{i-1}^{i-1}R$ and ${}_{i-1}^{i-1}P$ represent the rotation transformation matrix and the translation transformation matrix of the coordinate system $\{O_i\}$ relative to $\{O_{i-1}\}$, respectively, and a_i is equal to L_{i-1} , which is the translation distance of the coordinate system.

Table 1. D-H parameters of the HRM.

Coordinate System $\{O_i\}$	$a_i(\text{mm})$	$\theta_i(\text{°})$	$\alpha_i(\text{°})$	$d_i(\text{mm})$
0	x_0	0	0	0
1	0	θ_1	α_1	0
2	$L_1 = 486$	θ_2	α_2	0
3	$L_2 = 486$	θ_3	α_3	0
4	$L_3 = 486$	θ_4	α_4	0
5	$L_4 = 486$	θ_5	α_5	0
6	$L_5 = 486$	θ_6	α_6	0
7	$L_6 = 206$	θ_7	α_7	0
8	$L_7 = 206$	θ_8	α_8	0
9	$L_8 = 284$	0	0	0

In this paper, the links are connected through a universal joint that can rotate in both the pitch and yaw directions. In other words, the i th universal joint has two degrees of freedom, θ_i and α_i , which can be converted into the link angle ψ_i (link angle is the angle between the axes of adjacent links) and position angle γ_i (position angle is the angle between the projection line of the posterior link on the vertical surface of the preceding link and the horizontal line) to analyze the relationship of the location between adjacent links. The relationship between the joint angle and link angle can be observed in Figure 2, and the following conversion equation can be obtained.

$$\psi_i = \arccos[\cos(\theta_i) \cdot \cos(\alpha_i)] \in [0, 42.5^\circ], \tag{2}$$

$$\gamma_i = \arctan\left[\frac{-\sin(\theta_i)}{\cos(\theta_i) \cdot \sin(\alpha_i)}\right] \in [-90^\circ, 90^\circ], \tag{3}$$

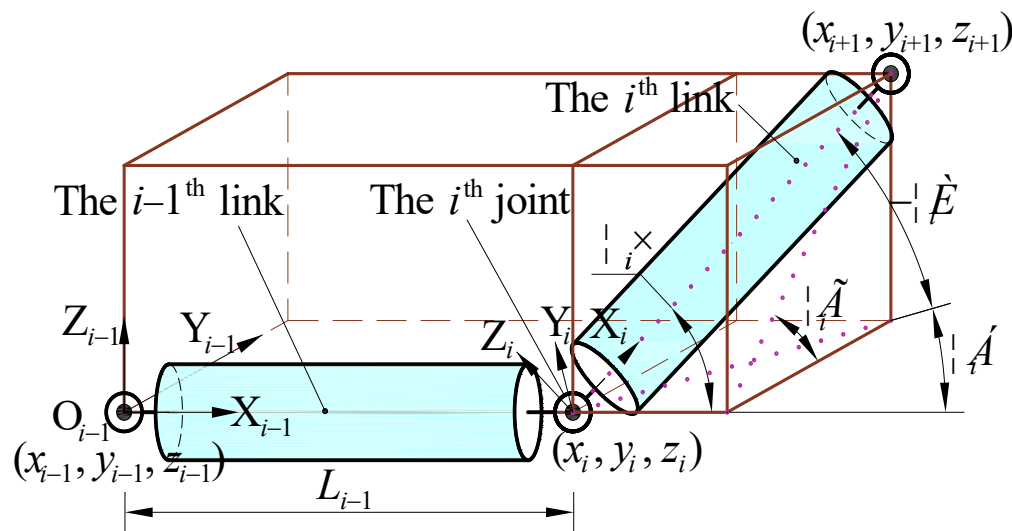


Figure 2. Schematic diagram of the joint angle and link angle.

Through the transformation matrix, the mapping relationship among the length of the driving cable, joint angle, and the position of the end-effector of each link can be analyzed, which is introduced in Section 5.

Solving each joint angle and an overall translation distance by the position of the end-effector (x_9, y_9, z_9) required three given equations to obtain 17 parameters, corresponding to an infinite number of solutions. To solve the non-uniqueness, reduce the complexity of the inverse kinematics of HRM, and realize the performance of obstacle avoidance, a novel

method of path planning and solving inverse kinematics, variable dimensional scaling method (VDSM), is proposed in this paper.

3. Principle of VDSM without Obstacles

3.1. General Framework of VDSM

The VDSM flowchart presented in this article is shown in Figure 3.

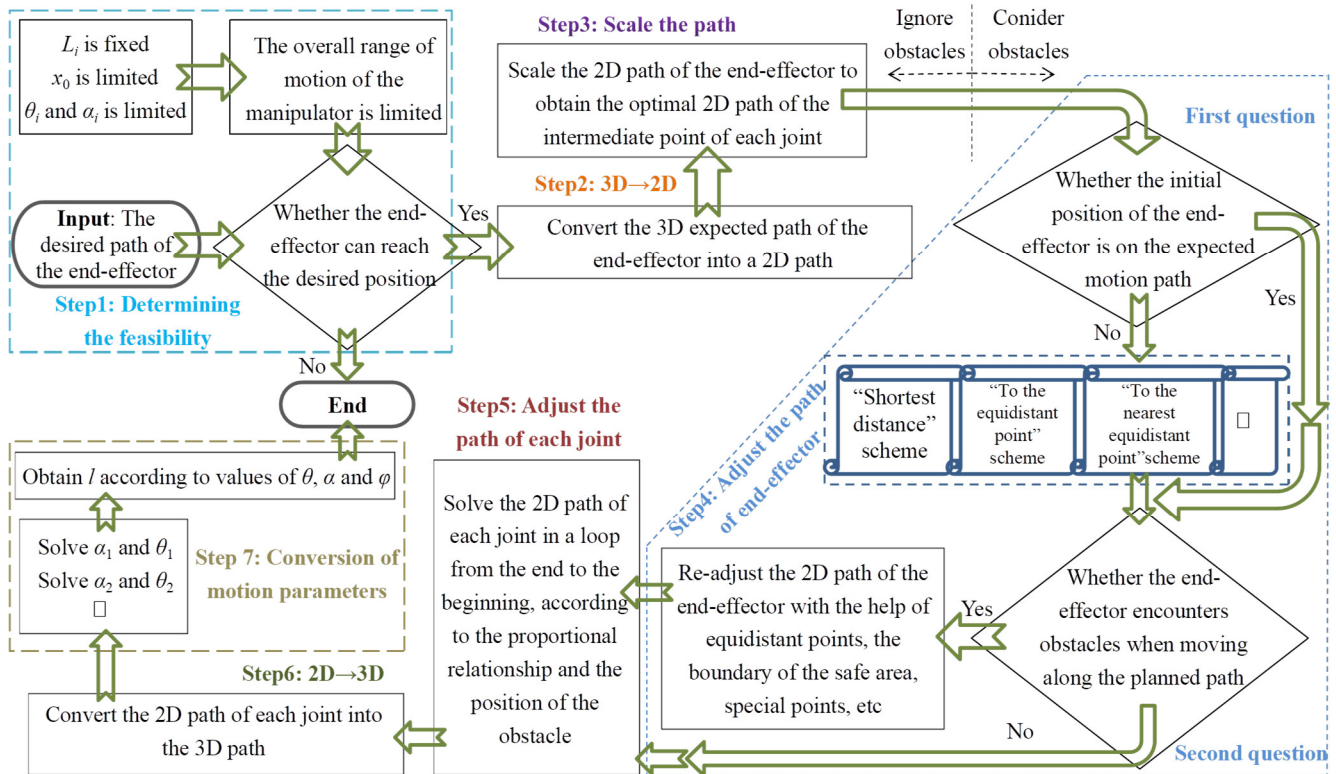


Figure 3. Flow chart of VDSM.

In this paper, by taking the way in which the end-effector moves along the 1500×1500 square on the plane $X_0 = \sum_{w=1}^8 L_w = 3126$ as an example, the principle of the VDSM is described specifically with no obstacles and three different obstacles.

Firstly, the principle of VDSM is analyzed when there is no obstacle. As can be observed in the flow chart, the influence of obstacles does not need to be considered in Step 1, Step 2, and Step 3 of the VDSM. The principle of these three steps is described successively as follows.

3.2. Step 1: Determining the Feasibility

The range of parameters of the manipulator is limited, which limits the overall range of motion of the manipulator. The motion range of the HRM in this paper can be regarded as unrestricted in the range of the X_0 axis, and the motion range in the plane Y_0Z_0 is in a circle with the projection of the X_0 axis on the plane as the center r_{yz} as the radius. In this paper, if $\psi_i \leq 42.5^\circ$, the maximum distance between the end of the manipulator and the X_0 axis, that is, the motion radius $r_{yz} = 2966$ mm, can be obtained by the following equation:

$$\begin{aligned}
 r_{yz} &= L_1 \cdot \max(\sin(\psi_1)) + L_2 \cdot \max(\sin(2 \cdot \psi_2)) + \sum_{i=3}^8 L_i \cdot \max(\sin(i \cdot \psi_i)) \\
 &= L_1 \cdot \sin(42.5^\circ) + L_2 \cdot \sin(85^\circ) + \sum_{i=3}^8 L_i \cdot \sin(90^\circ)
 \end{aligned}
 \tag{4}$$

This step is required to determine whether the end-effector can reach the desired position without considering obstacles according to the motion range of the HRM. If positive, proceed to the next step. If negative, terminate the algorithm.

3.3. Step 2: 3D→2D

Because the manipulator as a whole has translational degrees of freedom along the X_0 axis, its motion range is not limited. However, there are no overall translational degrees of freedom in the Y_0 axis and Z_0 axis directions, and the range of motion is limited. By taking advantage of the flexibility of the X_0 axis, the 3D problem can be projected along the X_0 axis at first, and then transformed into a 2D problem to reduce the complexity of solving the inverse kinematics.

The expected 3D path of the end-effector is projected on the plane Y_0Z_0 in this step. In other words, the planned 3D path of the end-effector is transformed into a 2D path, which lays a foundation for the path planning of the center point of the intermediate joint.

3.4. Step 3: Scale the Path

In this step, the 2D path of the end-effector is scaled to obtain the 2D reference path of the center point of each intermediate joint.

Depending on the length of each link, a definite scaling relationship can be obtained. When not considering obstacles, the 2D path of the end-effector is employed to calculate the 2D path of all center points of the joint projected on the Y_0Z_0 plane. In this step, only the best 2D motion path of each joint center is obtained without considering obstacles, which provides references for better accommodation under circumstances with obstacles. For example, the 2D practical path of each joint is limited to no more than the 2D reference path in obs2.

3.5. Scaling Relationship

In this section, the scaling relationship among the 2D motion paths of each joint center point is described, and according to the scaling relationship, the 2D motion of each joint center point considering no obstacle is solved; then, the 3D motion paths of all joint center points are planned. The long links are shown in purple, and the three short end links are shown in blue.

The motion path of the end-effector O_9 draws the black square wire frame shown in Figure 4 on the plane $X_0 = \sum_{w=1}^8 L_w = 3126$. The rotation center of the first joint O_1 can only move along the X_0 axis, so the projection of its path along the X_0 axis is a point.

To solve the problem of non-uniqueness and complexity of solving the inverse kinematics, the projection of the path of the rotation center point O_1 – O_8 from the first joint to the eighth joint along the X_0 axis and the path of the end-effector are defined as a certain scaling ratio k_{1_9} – k_{8_9} , which are related to the length of the link L_i , as shown in Equation (5). It can be seen, in the equation, that the value of k_{i_9} is between 0 and 1.

$$k_{i_9} = \begin{cases} 0, i = 1 \\ \left(\sum_{w=1}^{i-1} L_w \right) / \left(\sum_{w=1}^8 L_w \right), i = 2, 3, 4 \dots 9 \end{cases} \quad (5)$$

The above equation only analyzes the scaling relationship k_{i_9} between the position of the i th joint center point and the position of the end-effector, and the denominator is the total length of all links. According to this equation, the scaling relationship k_{i_j} between

the position of the i th joint center point and the position of the j th joint center point can be deduced:

$$k_{i-j} = \begin{cases} 0, i = 1, i \neq j \\ \left(\sum_{w=1}^{i-1} L_w \right) / \left(\sum_{w=1}^{j-1} L_w \right), i = 2, 3, 4 \dots 9, j = 2, 3, 4 \dots 9, i \neq j \\ 1, i = j \\ \infty, j = 1, i \neq j \end{cases}, \quad (6)$$

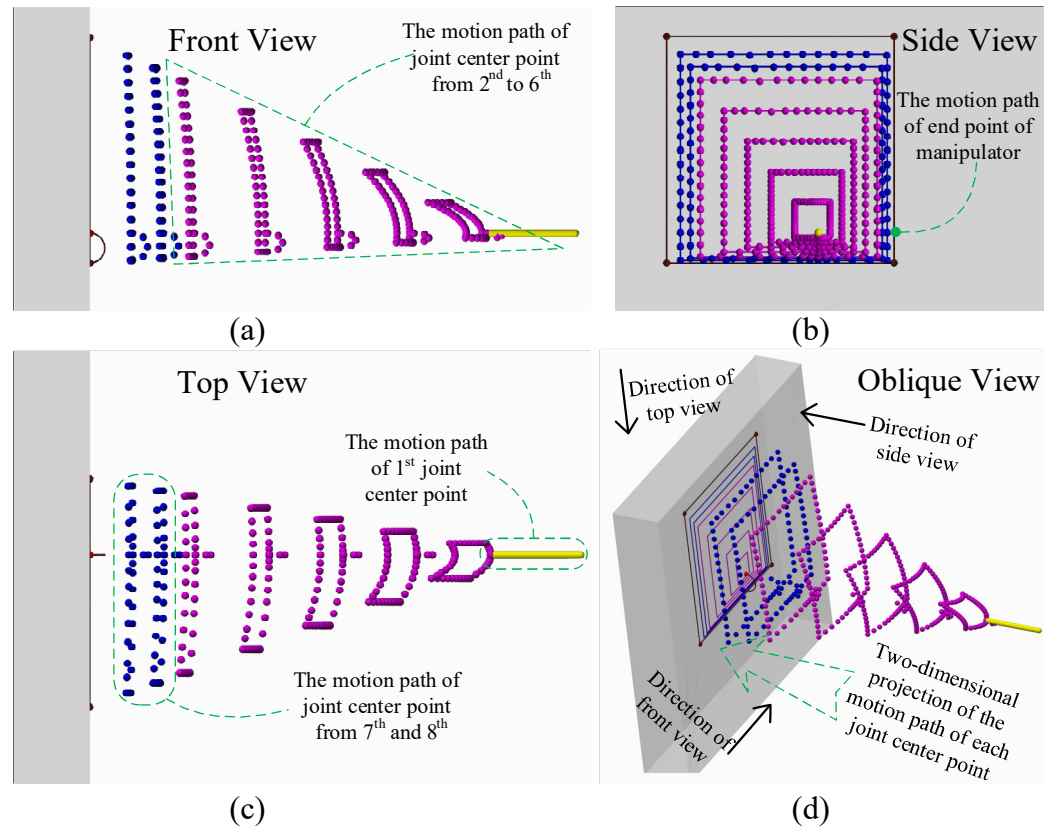


Figure 4. The 3D paths and 2D projections of all joint center points. (a) Front view; (b) Side view; (c) Top view; (d) Oblique view.

According to the above relationship of the scaling ratio, the 2D path projected by all joint nodes on the Y_0Z_0 plane can be planned according to the 2D path of the end-effector. According to the length L_i of each link, the 3D path of all joint center points from the end-effector to the first joint center point can be obtained. For example, given the 3D coordinates $(x_{i+1}, y_{i+1}, z_{i+1})$ of the $(i + 1)$ th joint center point O_{i+1} , the specific values of the 3D coordinates (x_i, y_i, z_i) of the i th joint center point O_i can be obtained using Equation (7). The 3D and 2D projection diagrams of the paths of all joint center points are shown in Figure 4.

$$\begin{cases} y_i = y_{i+1} \cdot k_{i-i+1} \\ z_i = z_{i+1} \cdot k_{i-i+1} \\ x_i = x_{i+1} - \sqrt{L_i^2 - (y_{i+1} - y_i)^2 - (z_{i+1} - z_i)^2} \end{cases}, \quad (7)$$

Figure 4 shows the 3D view and oblique view of the motion path of each joint center point, in which each ball represents the discrete point passed by the joint center point. The side view in Figure 4b and the oblique view in Figure 4d also include 2D projections of the motion paths of each joint center point. It can be seen from Figure 4b that the 2D projection paths of all joint nodes are square paths. However, except for the motion path of

the end-effector of the manipulator and the center point of the first joint, the 3D paths of the other joint nodes are curves. It can be seen from Figure 4a,c that the bending radius of the 3D path at the front joint center point is larger, while the bending radius of the 3D path at the back joint center point is flatter.

When there is no obstacle, the inverse kinematics are solved by using the VDSM, and the result is that the eight links are always coplanar. The method adopts as few degrees of freedom as possible to achieve the motion of the end-effector on the expected path, and the previous degrees of freedom are changed in priority: the translational degree of freedom x_0 , the rotational degree of the first joint θ_1 and α_1 , the rotational degree of the second joint θ_2 and α_2 , and so on.

In the example without obstacles, only three degrees of freedom, x_0 , θ_1 , and α_1 , are changed, while the remaining angles remain as zero. In other words, only the overall translational position x_0 of the manipulator and the first link angle ψ_1 are changed and the other seven link angles ψ_2 – ψ_8 remain as zero. The angle corresponding to each degree of freedom should be zero as much as possible to achieve the desired motion of the end-effector when fewer joint angles are changed.

4. Principle of VDSM with Obstacles

4.1. Obstacle Models

If there are obstacles and the path is still planned according to VDSM, without considering the obstacles in Section 3, the collision shown in Figure 5 will occur. When the end-effector moves to point (3126, 1000, 1300), the manipulator will interfere with these three obstacles. Obstacles of the first kind (obs1) are cylindrical, with a radius of 200 located at $(x, 700, 600)$. The second type of obstacle (obs2) is a triangular prism obstacle with a tangent circle whose radius is 200 located at $(x, 400, 400)$. Obstacles of the third kind (obs3) are cylindrical with a radius of 200 located at $(2126, 600, z)$.

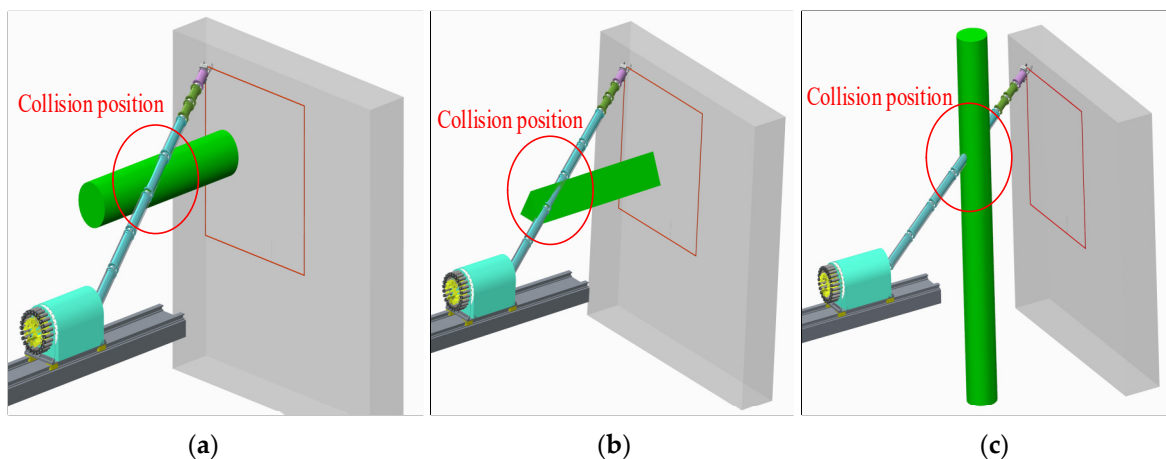


Figure 5. Three kinds of obstacle models and collision scenarios. (a) Obs1: first obstacle; (b) Obs2: second obstacle; (c) Obs3: third obstacle.

For different obstacles, the VDSM without considering obstacles needs to be strengthened according to the specific obstacle model to make each joint center point of the HRM move along the final planned path while retaining the advantages of the VDSM without obstacles.

In Step 4, Step 5, and Step 6 of the VDSM, the influence of obstacles should be considered. The principle of these three steps is described as follows:

4.2. Step 4: Adjust Motion Path of End-Effector

4.2.1. Two Kinds of Problems

When the expected path of the end-effector is known, the following problems need to be analyzed:

- (1) Whether the initial position of the end-effector is located on the desired motion path must be considered. If not, the corresponding path should be planned so that the end-effector moves from the initial position to the desired path without encountering obstacles and the preliminary motion position of the end-effector on the desired path should be determined;
- (2) Whether the end-effector will encounter obstacles as it moves along the planned path needs to be defined. If the end-effector encounters obstacles, the path of the end-effector should be adjusted.

This step is divided into several different methods according to the position, shape, size, and initial position of the obstacle to expand the expected path of the end-effector to the actual motion path.

The parameters of three kinds of obstacles were established in the obstacle model. In this paper, the initial state of the HRM was horizontal, and the end-effector of the manipulator was located at point (3126, 0, 0). After projection, it was divided into the points shown in Figure 6 as A_1 and B_1 . The expected path of the end-effector is to draw a 1500×1500 square on the plane $X_0 = 3126$, as shown in the black square at the outermost end of the image. The four vertices of the square in Figure 6a are A_3 , A_6 , A_7 , and A_8 . The obstacles are indicated by green entities. Because of the diameter of the manipulator and the influence of various errors, the safety distance between each joint center of the HRM and the obstacles should be set. The green area around the obstacles in Figure 6 (projected as the green curve) is the corresponding safe range, and the path is planned as far from the surface as possible. The red points in Figure 6 are the starting points or equidistant points in the end path of the manipulator, and the red line segments in the figure are the auxiliary lines for finding equidistant points.

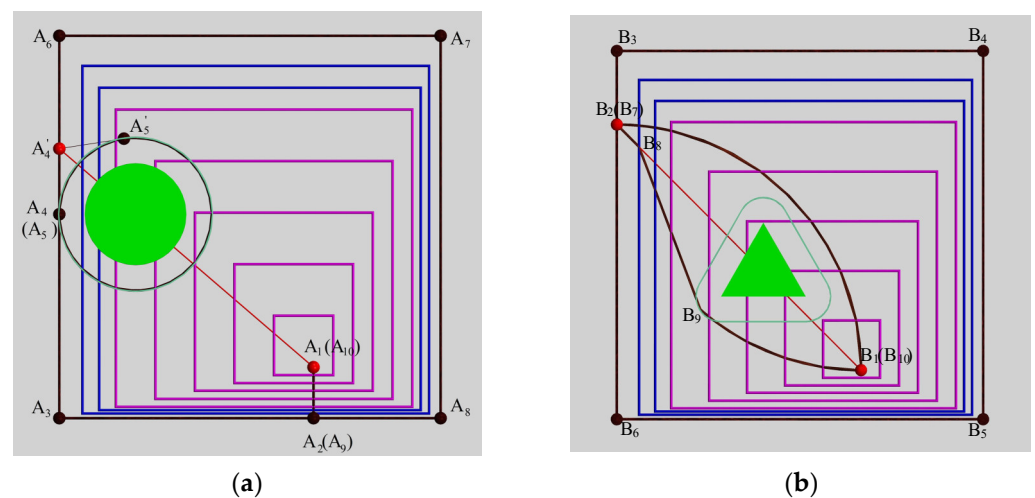


Figure 6. Motion path of the end-effector. (a) 2D path of end-effector of the manipulator in obs1; (b) 2D path of end-effector of manipulator in obs2.

4.2.2. Solution to the First Problem

For the first kind of problem, the path can be planned based on various optimizing indexes or projects. In this paper, the initial position of the end-effector does not fall within the expected path, so it is necessary to design a corresponding plan to make the end-effector move from the initial position to the expected path. The three schemes: “Shortest distance”, “To the equidistant point”, and “To the nearest equidistant point” are described in detail hereinafter.

The “Shortest distance” scheme is to identify a point closest to the end-effector of the manipulator on the expected path. The path is then planned from the initial position to the nearest point without touching obstacles. The movement from point A_1 to point A_2 in Figure 6a is an example.

The “to the equidistant point” scheme aims to find the only equidistant point on the expected path, and then the path is planned from the initial position to the nearest point without encountering obstacles. In obs1 and obs2, the preliminary position A_1 or B_1 is connected to O_{obs1} or O_{obs2} as the centroid projection point of the obstacle, and the connecting line is extended. The point where the extension line intersects the desired path is the equidistant point. The equidistant point refers to the point on the projection plane perpendicular to the centerline of the obstacle where the distances for reaching the point in two directions equally. For example, both points A'_4 in Figure 6a and B_2 (B_7) in Figure 6b are equidistant points. The path can be planned from the initial position along the border of the obstacles to the equidistant path when the equidistant points are found in obs2, and paths of other forms can also be planned. In this paper, the complexity of the path is simplified on the premise of guaranteeing that no obstacle is encountered. In this way, the movement in the arc paths above the obstacles from point B_1 to point B_2 is planned, similar to the paths below the obstacles from point B_7 to point B_8 . However, there are sometimes multiple obstacles and multiple equidistant points; the “nearest equidistant point” scheme is then needed.

The scheme of “to the nearest isometric point” aims to find the nearest isometric point in several isometric points and then plan the path from the initial position to the nearest point without encountering obstacles.

4.2.3. Solution to the Second Problem

For the second kind of problem, if there is no obstacle encountered in any place by the manipulator during the whole movement process, the path of the center point of each joint can be planned according to the basic VDSM without considering obstacles. Then, the inverse kinematics of the HRM can be solved and the variation law of each degree of freedom can also be obtained. If an obstacle is encountered, the 2D path of the end-effector will be readjusted based on the principle of the VDSM to prepare for adjusting the 2D path of each joint in the next step. Based on the above process, obstacle avoidance can be achieved and the end-effector can complete the task of moving along the desired path.

The obstacles are taken as examples to explain how to adjust the motion path of the end-effector. To avoid encountering obs1, the end-effector can be moved along the following 2D points: $A_1-A_2-A_3-A_4-A'_4-A_5-A'_5-A'_4-A_6-A_7-A_8-A_9-A_{10}$, where the arc from point A_5 to point A'_5 is the circular arc in the counterclockwise direction in Figure 6a. Although the equidistant point A'_4 is used in the planned path, the path is relatively complex and requires some additional calculations (such as calculating the position of points, etc.). In order to simplify the complexity of the motion path of the end-effector, the 2D motion path of the end-effector is changed to $A_1-A_2-A_3-A_4-A_5-A_6-A_7-A_8-A_9-A_{10}$, and the path from point A_4 to point A_5 is a counterclockwise circle around the obstacle in Figure 6a. In the next step, it will be presented in detail whether the HRM can move to point A_4 (point A_5) bypassing the obstacle. In obs2, the 2D motion path of the end-effector can be planned as $B_1-B_2-B_3-B_4-B_5-B_6-B_7-B_8-B_9-B_{10}$, where point B_1 to point B_2 and point B_9 to point B_{10} are two arcs in Figure 6b. The motion path of section $B_7-B_8-B_9$ is planned to reduce the deflection range of the link angle. In obs3, the 2D motion path of its end-effector is the same as that of the end-effector without obstacles, and the 2D motion path can be expressed as $A_1-A_2-A_3-A_6-A_7-A_8-A_9-A_{10}$ in Figure 6a.

In the process of the end-effector moving from the initial position to the desired path (for example, from point A_1 to point A_2), and in the process of moving away from the desired path to avoid obstacles (for instance, from point A_4 to point A_5). The x -coordinate of the end effector (x_9) can be appropriately reduced based on planning the two coordinates of y_9 and z_9 to prevent the end-effector from scratching the plane $X_0 = 3126$.

In this step, the motion path of the end-effector is adjusted according to the obstacles. In the next step, the movement path of each joint center point is adjusted to achieve the purpose of bypassing the obstacle.

4.3. Step 5: Adjust Path of Each Joint

The motion path of the end-effector can be adjusted through Step 4. The HRM may encounter obstacles if the path of each joint is not adjusted.

Assume that the 2D projection positions of the end-effector O_9 and the center points O_8-O_1 of each joint are $P_9, P_8 \dots P_1$. If the location of the end-effector $O_9 (x_9, y_9, z_9)$ is known, according to the proportional relationship and the position of the obstacle, point P_8 can be obtained, then point P_7 can be obtained, and so on until the position of point P_1 can be obtained. Figure 7 shows the 2D projection diagram of the manipulator when the end-effector is located at A_4 and A_5 , respectively. In this method, the 2D projection positions of the center points of each joint are first calculated in the 2D projection plane, and then the 3D position of each point is calculated according to the length of each link. Next, how to solve the 2D projection positions of each joint center point successively for different types of obstacles is described. Because the manipulator in this paper has a translational degree of freedom in the direction of the X_0 axis, the 2D projection for point O_1 is constant as point P_1 .

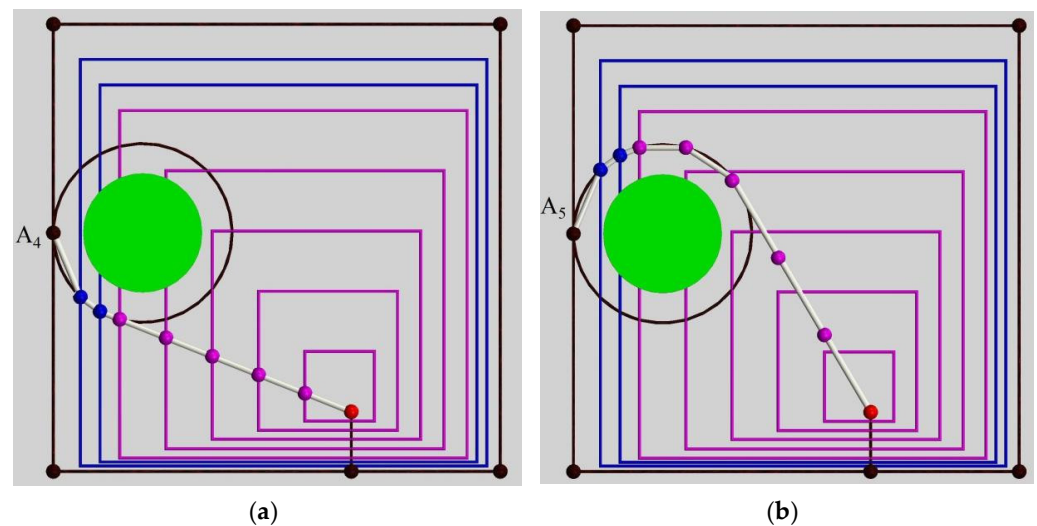


Figure 7. Two-dimensional projection diagram of the manipulator. (a) End-effector is located at A_4 ; (b) End-effector is located at A_5 .

As an example, the end of the effector at point P_9 in Figure 8 is used to describe how to obtain the position at points P_8-P_2 successively, which corresponds to the situation where the location of the end-effector is affected by the obstacles. Point P'_8 can be obtained by connecting point P_1 to point P_9 and adopting the proportional relation as the following equation:

$$\overline{P_1P'_8} = k_{8_9}\overline{P_1P_9} = \left[\left(\sum_{w=1}^7 L_w \right) / \left(\sum_{w=1}^8 L_w \right) \right] \overline{P_1P_9}, \tag{8}$$

It can be seen from Figure 8a that point P'_8 is not within the safe range, so it is an infeasible point. A horizontal line and a vertical line are drawn to cross the point, and the expected path intersects at four points. According to these four points, the point nearest to the position of the former point on P_8 is selected as the current final P_8 point.

In addition to drawing auxiliary lines, such as a “positive cross” to find the intersection, an “oblique cross” or a circle of radius $\overline{P_1P'_8}$ through point P_1 can be employed to find the intersection point. However, when adopting the latter two methods, the link angle will be larger. Therefore, a horizontal line and a perpendicular line are selected to adjust the position of the center point of the joint in this paper.

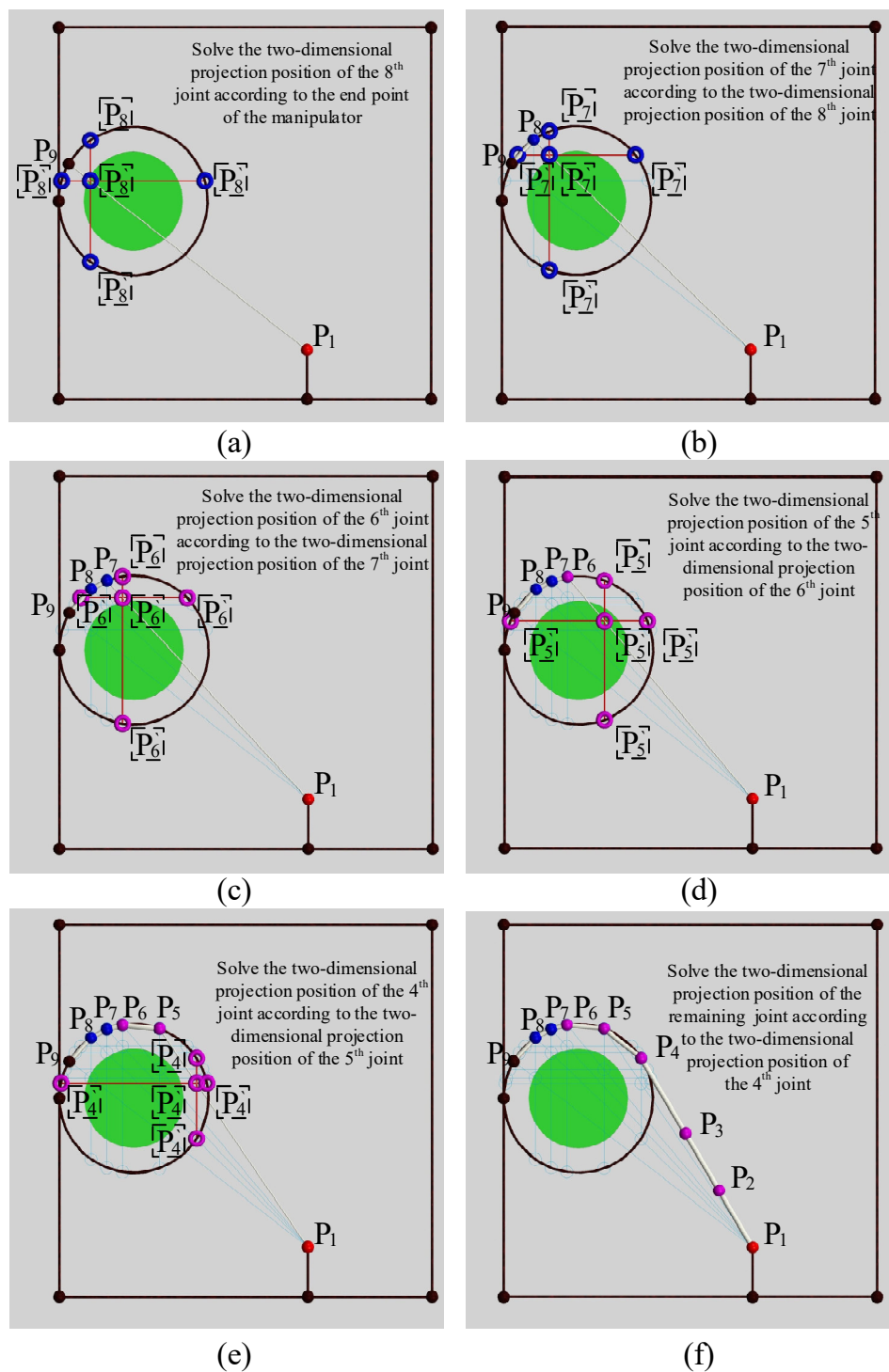


Figure 8. Process of solving the 2D projection positions of center points of each joint. (a) Solve 2D projection position of the 8th joint; (b) Solve 2D projection position of the 7th joint; (c) Solve 2D projection position of the 6th joint; (d) Solve 2D projection position of the 5th joint; (e) Solve 2D projection position of the 4th joint; (f) Solve 2D projection position of remaining joint.

After the projection P_8 of the eighth joint is obtained, points P_1 and P_8 are connected. Then, point P_7 can be obtained by using the proportion relation as the following equation:

$$\overline{P_1P_7} = k_{7,8}\overline{P_1P_8} = \left[\left(\sum_{w=1}^6 L_w \right) / \left(\sum_{w=1}^7 L_w \right) \right] \overline{P_1P_8}, \tag{9}$$

It can be seen from Figure 8b that the middle point P'_7 is not within the safe range, so it is an infeasible point. A horizontal line and a vertical line are drawn to cross the point, which intersect with the expected path at four points. According to these four points, the point closest to the position of the anterior point on P_7 is selected as the final point P_7 .

Points P_6 , P_5 , and P_4 can be calculated by analogy. After obtaining point P_4 , point P'_3 can be obtained by connecting point P_1 to point P_4 and utilizing the proportional relation as the following equation:

$$\overline{P_1 P'_3} = k_{3_4} \overline{P_1 P_4} = \left[\left(\sum_{w=1}^2 L_w \right) / \left(\sum_{w=1}^3 L_w \right) \right] \overline{P_1 P_4}, \quad (10)$$

As can be seen from Figure 8f, point P'_3 is within the safety range and can be regarded as the final P_3 point.

As shown in Figure 8, the successful solution of the 2D projection positions of the center points of each joint is described when the end-effector is known to be at a specific discrete point. In Figure 9, by taking the end-effector moving from point A_5 to point A_6 as an example, it can be demonstrated how the VDSM can be used to solve the 2D projection positions of the center points of each joint during the movement process.

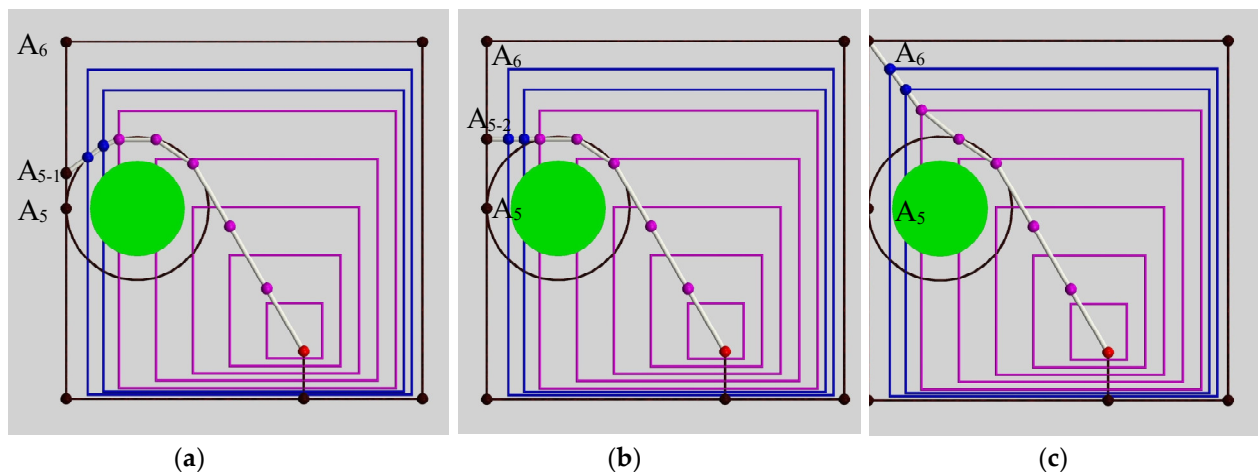


Figure 9. Two-dimensional projection diagrams of the process of the manipulator when the end-effector moves from A_5 to A_6 . (a) End-effector is located at A_{5-1} ; (b) End-effector is located at A_{5-2} ; (c) End-effector is located at A_6 .

When the end-effector moves from point A_5 to point A_{5-1} , only the 2D projection position of the end-effector changes, while the positions of the center points of the other eight joints remain unchanged. When the end-effector moves from point A_{5-1} to A_{5-2} , in addition to the effector at the end of the 2D projection position changing, the eighth joint center of the projection position also changes, and the seventh joint center of the projection position also changes after a while. However, the projection positions of the six joint centers in the front remain unchanged. In the process of the end-effector moving from point A_{5-2} to point A_6 , the 2D projection position will always move along a vertical line. The projection positions of the center points of other joints are also on a corresponding vertical line all the time. By analyzing the above process, it can be concluded that the manipulator always conforms to the principle of the VDSM.

4.4. Step 6: 2D→3D

In the previous step, the final 2D projection position of each joint center can be solved by analyzing the position and proportion coefficient of the end-effector and whether the joint center point is in the safe range. In this step, the 3D position and 3D path of each joint

center can be successively solved by Equation (7), and the 2D path between the end-effector and each joint center can then be converted into a 3D path.

In this step, the 3D motion paths of the end-effector and the center points of each joint can be planned. Next, on the premise that the 3D path is known, the inverse kinematics are solved through Step 7 to build a mapping model among the coordinate points, angle of each joint, and length of each driving cable.

5. Conversion of Motion Parameters

After the 3D position and the 3D path of each node are obtained, the variation law of the pitch angle θ_i and yaw angle α_i of each joint can be obtained from the initial joint successively through the position parameters. Finally, the angle is converted to the length of the driving cable. The following is a detailed explanation of the mapping relationship between the parameters.

5.1. Mapping Relationship between Angles and Coordinates

The coordinates (x_i, y_i, z_i) ($i = 1, 2, \dots, 9$) of all key points O_i can be obtained by following the previous steps. First, α_1 and θ_1 can be obtained from (x_1, y_1, z_1) and (x_2, y_2, z_2) , and the equation is as follows:

$$\theta_1 = \arcsin \frac{-(z_2 - z_1)}{L_1} \in [-42.5^\circ, 42.5^\circ], \quad (11)$$

$$\alpha_1 = \arcsin \frac{y_2 - y_1}{L_1 \cdot \cos \theta_1} \in [-42.5^\circ, 42.5^\circ], \quad (12)$$

The value of α_1 and θ_1 can be solved in the natural coordinate system. However, α_2 and θ_2 are the deflection angle of the second link with respect to the first link, instead of the angle of the second link in the natural coordinate system. Therefore, when solving the deflection angle of the i th link with respect to the $(i - 1)$ th link, the coordinate points need to be converted from the natural coordinate system to the coordinate system $\{O_{i-1}\}$ of the $(i - 1)$ th link.

$$\begin{bmatrix} x_{i+1_{i-1}} \\ y_{i+1_{i-1}} \\ z_{i+1_{i-1}} \\ 1 \end{bmatrix} = {}^{i-1}_{i-2}T \cdot {}^{i-2}_{i-2}T \cdots {}^1_0T \cdot \begin{bmatrix} x_{i+1} \\ y_{i+1} \\ z_{i+1} \\ 1 \end{bmatrix}, \quad (13)$$

where $(x_{i+1_{i-1}}, y_{i+1_{i-1}}, z_{i+1_{i-1}})$ is the coordinate of the i th link end point O_{i+1} in the coordinate system $\{O_{i-1}\}$. The coordinate in the coordinate system $\{O_{i-2}\}$ can be converted to the coordinate system $\{O_{i-1}\}$ through ${}^{i-1}_{i-2}T$. The matrix ${}^{i-1}_{i-2}T$ is the inverse matrix of the matrix ${}^{i-2}_{i-1}T$, which contains three parameters, α_{i-1} , θ_{i-1} , and L_{i-1} .

The deflection angles α_i and θ_i of the i th link relative to the $(i - 1)$ th link can be obtained by $(x_{i+1_{i-1}}, y_{i+1_{i-1}}, z_{i+1_{i-1}})$, and the specific equations are as follows:

$$\theta_i = \arcsin \frac{-z_{i+1_{i-1}}}{L_i} \in [-42.5^\circ, 42.5^\circ], \quad (14)$$

$$\alpha_i = \arcsin \frac{y_{i+1_{i-1}}}{L_i \cdot \cos \theta_i} \in [-42.5^\circ, 42.5^\circ], \quad (15)$$

The 16 deflection angles can be successively solved according to the above equation and can be converted into eight link angles with the introduction of Section 2.

5.2. Mapping Relationship between Cable Length and Angles

The deflection angle of each joint can be obtained by the coordinates of each joint position; then, the length of each driving cable at the joint can be obtained by the deflection

angle of each joint and, next, the total length of each driving cable can be obtained by the sum.

In this paper, each joint of the manipulator is driven by three parallel driving cables. One end of the driving cable is fixed to the end face of the joint, and the other end is fixed to the driving mechanism of the base. Under the limitation of the universal joint, the link can be pulled by the driving cable to rotate the joint. There are $27-3i$ ($i = 1, 2, \dots, 7, 8$) driving cables passing through the i th link, but only 3 driving cables are used to drive this link, with the rest of the driving cables passing through this link to drive the following link.

Taking the first joint as an example, the relationship between the lengths of the 24 driving cables at the joint, α_1 , θ_1 , and the position angle φ of the driving cable is analyzed. Figure 10 shows a schematic diagram of the placement of 24 cable holes, and the included angle between 2 adjacent cable holes is 15. Holes ija , ijb , and ijc represent the three holes on the i th ($i = 1, 2, \dots, 8$) link and are distributed into 120 uniformly. The three driving cables pass through holes ija , ijb , and ijc to drive the j th ($j = 1, 2, \dots, 8$ and $j \geq i$) link. When the position angle of each hole in Figure 10 is φ , the angle between the line, which is drawn by connecting the center of each hole and the center of the section, and the Z_i axis is the position angle φ of the point, so $\varphi_{15b} = 0$, $\varphi_{16b} = 15 \dots \varphi_{11a} = 180 \dots$, and $\varphi_{14b} = 345 = -15$.

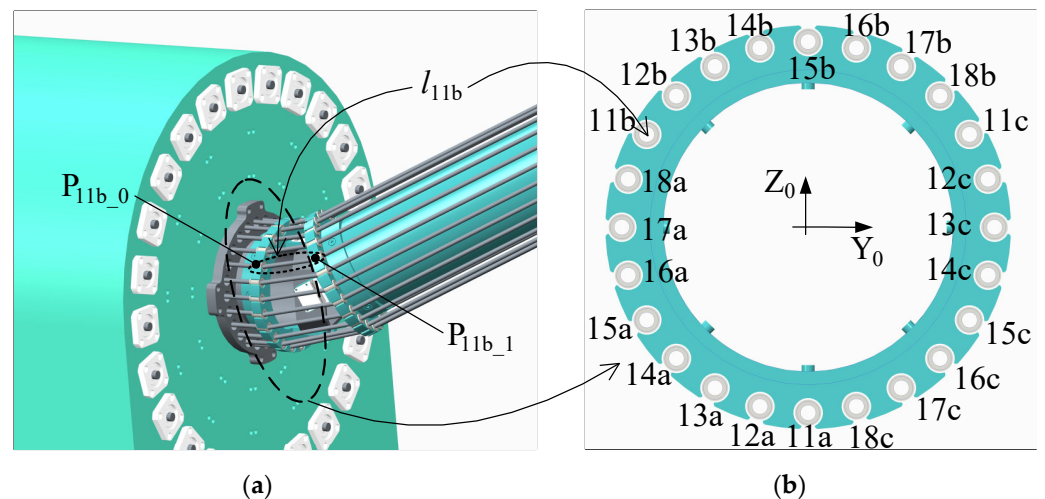


Figure 10. Schematic diagram of the distribution of ropes. (a) Oblique view at the first joint; (b) Distribution of driving cable.

The position of each point can be obtained by the position angle φ of each driving cable, which can be converted into the same coordinate system through coordinate transformation. Then, the distance between the two points can be obtained, and the mapping relationship between the length of the driving cable (l_{ija} , l_{ijb} , and l_{ijc}) and the joint angles (α_i and θ_i) of one joint can be obtained.

By solving the driving cable through hole 11b as an example, the calculation of l_{11b} is described. The position of point P_{11b_0} in the coordinate system $\{O_0\}$ is $(x_{11b_0}, y_{11b_0}, z_{11b_0})$, and according to the position angle φ_{11b} of hole 11b, the following can be calculated:

$$\begin{cases} x_{11b_0} = -d \\ y_{11b_0} = r \cdot \sin \varphi_{11b} \\ z_{11b_0} = r \cdot \cos \varphi_{11b} \end{cases}, \quad (16)$$

where d is the distance between the center point of the joint and the end face of the link and r is the distance between the center of the hole through which the driving cable passes and the center of the link.

The position of point P_{11b_1} in the coordinate system $\{O_1\}$ is $(x_{11b_1}, y_{11b_1}, z_{11b_1})$, and the position angle φ_{11b} of hole 11b can be obtained as follows:

$$\begin{cases} x_{11b_1} = d \\ y_{11b_1} = r \cdot \sin \varphi_{11b} \\ z_{11b_1} = r \cdot \cos \varphi_{11b} \end{cases}, \quad (17)$$

The position coordinates of point P_{11b_1} can be converted to the coordinate system $\{O_0\}$ through the transformation matrix 0_1T , and then the difference between point P_{11b_0} and point P_{11b_1} in three directions can be obtained by the following equation:

$$\begin{bmatrix} \Delta x_{11b} \\ \Delta y_{11b} \\ \Delta z_{11b} \\ 0 \end{bmatrix} = {}^0_1T(4 \times 4) \begin{bmatrix} x_{11b_1} \\ y_{11b_1} \\ z_{11b_1} \\ 1 \end{bmatrix} - \begin{bmatrix} x_{11b_0} \\ y_{11b_0} \\ z_{11b_0} \\ 1 \end{bmatrix}, \quad (18)$$

Then, the distance between point P_{11b_0} and point P_{11b_1} can be obtained:

$$l_{11b} = \overline{P_{11b_0}P_{11b_1}} = \sqrt{(\Delta x_{11b})^2 + (\Delta y_{11b})^2 + (\Delta z_{11b})^2}, \quad (19)$$

After derivation,

$$\begin{aligned} l_{11b}^2 &= (d \cdot c\alpha \cdot c\theta - r \cdot s\alpha \cdot s\varphi + r \cdot c\alpha \cdot s\theta \cdot c\varphi + d)^2 \\ &+ (d \cdot s\alpha \cdot c\theta + r \cdot c\alpha \cdot s\varphi + r \cdot s\alpha \cdot s\theta \cdot c\varphi - r \cdot s\varphi)^2 \\ &+ (-d \cdot s\theta + r \cdot c\theta \cdot c\varphi - r \cdot c\varphi)^2 \end{aligned} \quad (20)$$

where $\theta = \theta_1$, $\alpha = \alpha_1$, $\varphi = \varphi_{11b}$.

Equation (20) is a general equation. The real-time length of the driving cable at the joint can be obtained by inputting two deflection angles, θ and α , and the position angle φ of the driving cable. After solving the length of the driving cable at each joint and adopting the following equation to sum the length of each segment of the driving cable, the total length of each driving cable can be obtained:

$$\begin{cases} l_{ja} = \sum_{i=1}^j (l_{ija} + L_i - 2d) \\ l_{jb} = \sum_{i=1}^j (l_{ijb} + L_i - 2d) \\ l_{jc} = \sum_{i=1}^j (l_{ijc} + L_i - 2d) \end{cases}, \quad (21)$$

where l_{ja} , l_{jb} , and l_{jc} are respectively the total length of the three driving cables driving the j th link.

In short, the positions of the center points of joints can be deduced by the VDSM, then the angles of joints can be solved by the positions, and, finally, the lengths of 24 driving cables can be calculated by the angles.

6. Simulation Results

6.1. Three-Dimensional Motion Path

In the obstacle-free environment, the 3D motion path as shown in Figure 4 can be obtained by simulation with the VDSM. The motion paths of nine key points in three kinds of obstacle environments can be obtained by the simulation with the VDSM, as shown in Figures 11–13. Each figure is shown in four views from different perspectives. The path marked i th in Figures 11e–k and 12e–k is the movement path of the i th key point. In Figures 11–13, the black curve is the path of the end-effector, the two blue curves are the paths of the 7th and 8th joint center, the five pink curves are the paths of the 2nd to 6th joint

center, and the orange line segment is the path of the 1st joint center. The cyan translucent entity in Figures 11–13 is the obstacle.

It can be seen from Figures 11–13 that, after the motion path of the end-effector is planned, the 3D motion path of each joint center can be planned according to the VDSM in this paper. As can be seen from the side view, the motion paths of the nine key points had a certain proportional relationship with the 2D motion paths projected on the Y_0Z_0 plane. In obs3, the motion paths of the center points of each joint can be adjusted according to the VDSM in this paper when the manipulator moves somewhere between two boundaries to achieve the purpose of obstacle avoidance.

In obs1 and obs2, the 2D motion paths of the end-effector and the center points of each joint are adjusted according to the projection of the obstacle in the side view. In obs3, if it is far away from the obstacle, the 2D motion paths of the center points of each joint are adjusted in the side view. If the influence of the obstacle needs to be considered, the 2D motion paths of the center points of each joint are adjusted in proportion between the first boundary and the second boundary in the top view, the 3D movement path of each joint center point is then adjusted.

As can be seen from Figures 11–13, if the manipulator moves along the planned path, the end-effector can also move along the expected path without encountering the obstacle in three kinds of obstacle environments. By analyzing the 3D path of the HRM, it is proven that the VDSM achieved obstacle avoidance, variable dimension, constant ratio, simplification, non-iteration, and generality.

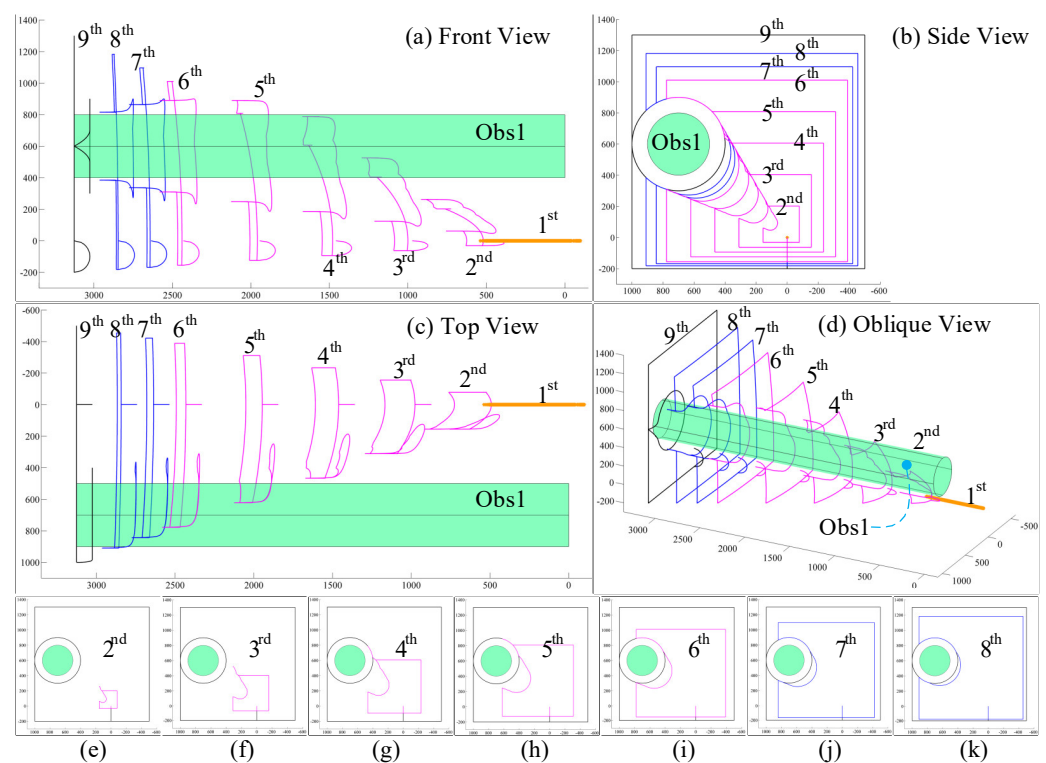


Figure 11. Motion paths of 9 key points in obs1. (a) Front view; (b) Side view; (c) Top view; (d) Oblique view; (e) Motion projection of 2nd joint; (f) Motion projection of 3rd joint; (g) Motion projection of 4th joint; (h) Motion projection of 5th joint; (i) Motion projection of 6th joint; (j) Motion projection of 7th joint; (k) Motion projection of 8th joint.

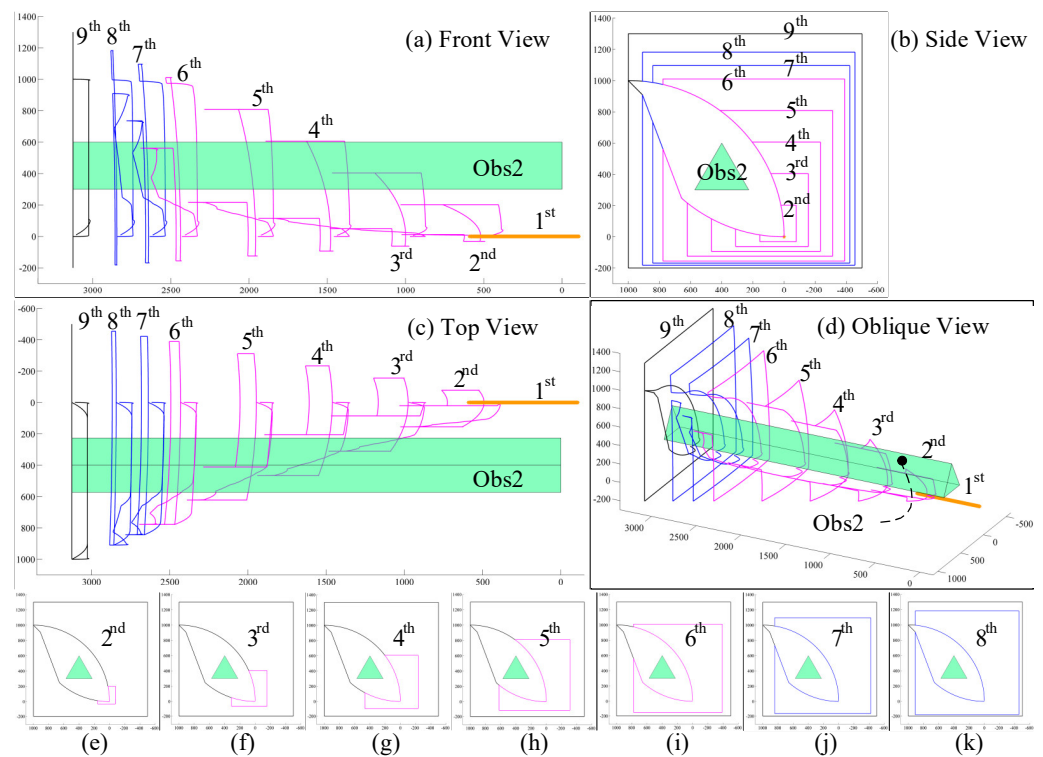


Figure 12. Motion paths of 9 key points in obs2. (a) Front view; (b) Side view; (c) Top view; (d) Oblique view; (e) Motion projection of 2nd joint; (f) Motion projection of 3rd joint; (g) Motion projection of 4th joint; (h) Motion projection of 5th joint; (i) Motion projection of 6th joint; (j) Motion projection of 7th joint; (k) Motion projection of 8th joint.

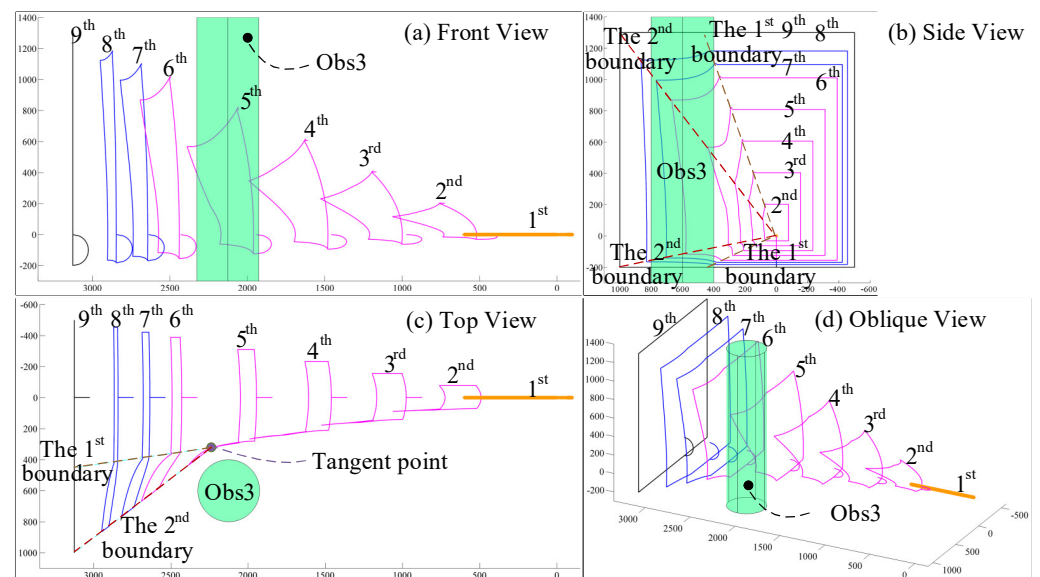


Figure 13. Motion paths of 9 key points in obs3. (a) Front view; (b) Side view; (c) Top view; (d) Oblique view.

6.2. Analysis of Simulation Results of Link Angle

6.2.1. Analysis of Whole Change Process of Link Angle

After the paths of the end-effector of HRM and the center point of each joint are planned, the coordinate value corresponding to the movement of the manipulator along the path can be converted into the angle of each joint, as introduced in Section 5. Then,

the change curves of the link angle of each joint under three kinds of obstacles or without an obstacle are obtained, as shown in Figure 14. The curves of eight link angles ψ_i and the overall translation distance x_0 of the manipulator changing with the position of the end-effector are shown. The actual coordinate of the point on curve x_0 in Figure 14 is 15 times the value shown on the coordinate axis in millimeters. The marked A_i and B_i correspond to point A_i and point B_i to which the end-effector of the manipulator moves, as shown in Figure 6.

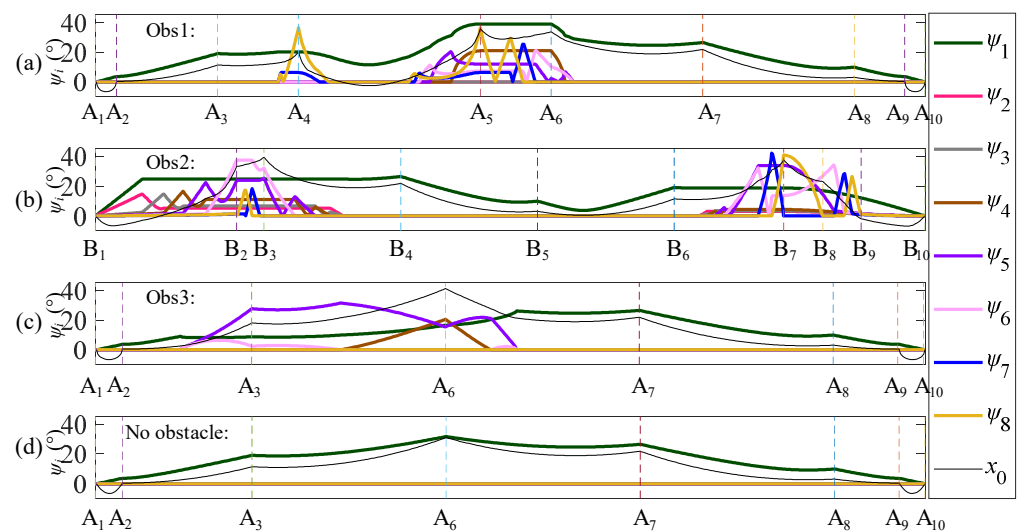


Figure 14. Variation curves of ψ_i and x_0 in four environments. (a) Parameter change curve in obs1; (b) Parameter change curve in obs2; (c) Parameter change curve in obs3; (d) Parameter change curve without obstacles.

As can be noted from Figure 14, many parameters changed to realize the function of the end-effector moving along the square trajectory while achieving obstacle avoidance. In the fourth figure, only x_0 and ψ_1 changed when it was obstacle-free, and the other seven link angles remained at zero. That is to say, the degree of freedom changed as little as possible to achieve the desired motion.

When there is no obstacle, only the two parameters x_0 and ψ_1 need to be changed, and the positions of the center points of each joint do not need to be adjusted. Therefore, auxiliary lines are not needed to adjust the position of the center points of each joint in Figure 8. However, when there are obstacles, auxiliary lines should be drawn around the obstacles to adjust the position of the center points of each joint to achieve the purpose of obstacle avoidance. For example: (1) in obs1, when the end-effector moves around point A_5 , the corresponding values of seven curves are not zero; only those of ψ_2 and ψ_3 are still zero, so five auxiliary lines are needed to search for points P_8 , P_7 , P_6 , P_5 , and P_4 at the boundary of the danger region. The process of drawing auxiliary lines is shown in Figure 8, which describes the process of solving the 2D projection positions of the center points of each joint. (2) In obs1, when the end-effector moves around point A_6 , as shown in Figure 9, the values corresponding to x_0 , ψ_1 , ψ_4 , ψ_5 , and ψ_6 are not zero, and two auxiliary lines are needed to find points P_5 and P_4 at the boundary of the danger region.

6.2.2. Change Rules of Link Angle with Obstacles

To achieve the expected motion of the manipulator under the premise of obstacle avoidance in the place affected by obstacles, not only do x_0 and ψ_1 need to be changed, but also the other seven link angles need to be changed. It can be seen from Figure 14 that the following places are affected by obstacles: (1) In obs1, the end-effector moves from point A_3 to point A_7 . (2) In obs2, the end-effector is in the process of moving from point B_1 to

point B_4 and from point B_6 to point B_{10} . (3) In obs3, the end-effector is in the process of moving from point A_2 to point A_7 .

The change rules of the link angle in the following five places are analyzed as follows: (1) In obs1, when the end-effector moves around point A_4 , only ψ_7 and ψ_8 are changed to avoid the manipulator impacting the obstacle. (2) As shown in Figure 15a, ψ_2 – ψ_8 are zero in the beginning. When the end-effector has moved around point A_5 , ψ_8 is first changed, then ψ_7 is changed, . . . ψ_4 is changed, making the five link angles change from zero to a non-zero value. During the process of the link angle returning to 0, ψ_8 first returns to zero, then ψ_7 returns to zero, and finally ψ_4 – ψ_6 return to zero. (3) As shown in Figure 15b, when the end-effector starts to move from point B_1 , ψ_2 – ψ_8 change slightly all at once firstly, and then ψ_2 – ψ_8 change sharply and separately. During the process the link angle returns to zero, ψ_8 – ψ_2 return to zero separately. (4) As shown in Figure 15c, the link angle is also regular and changes successively. (5) As shown in Figure 15d, ψ_4 – ψ_6 are changed in addition to changing x_0 and ψ_1 , while ψ_4 and ψ_6 will not be non-zero values at the same time during this process to avoid collision with the intermediate obstacle.

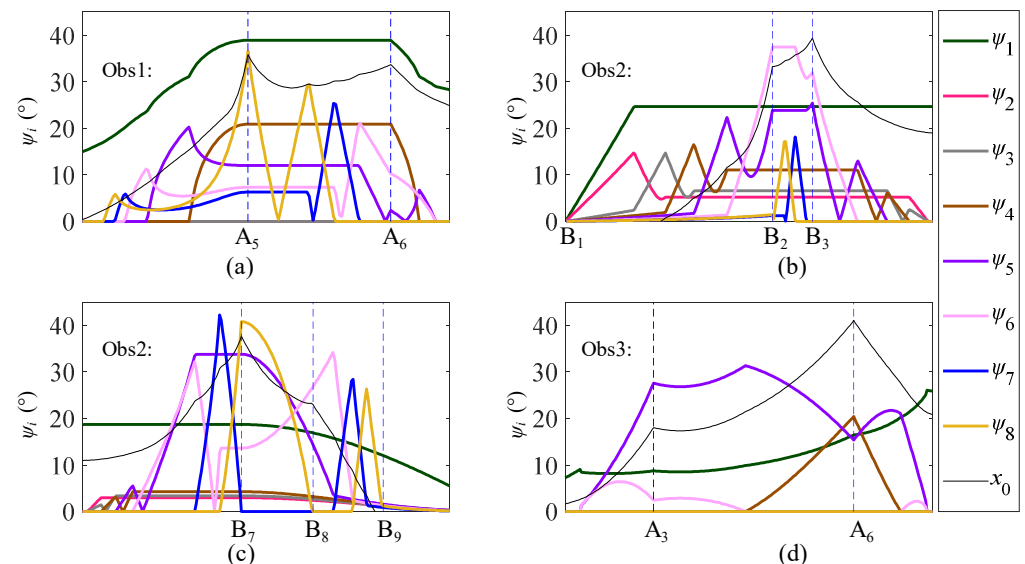


Figure 15. Local variation in the link angle at four positions. (a) The first partial enlargement of link angle; (b) The second partial enlargement of link angle; (c) The third partial enlargement of link angle; (d) The fourth partial enlargement of link angle.

6.2.3. Maximum of Each Link Angle

The variation curve of ψ_i and x_0 can be obtained through simulation; then, the corresponding variation range of ψ_i and x_0 can be sorted out, as shown in Figure 16. Acquired from Figure 16, when the end-effector moves between point A_1 and point A_2 , the minimum value of x_0 is -98 mm, while the corresponding maximum values of x_0 are 465 mm, 538 mm, and 591 mm, which indicates that, according to different obstacles, the overall motion range of the manipulator in the direction of the X_0 axis is uncertain. By changing x_0 , the link angle ψ_i can be reduced as much as possible.

In obs1, when the obstacle is far away from the X_0 axis, the two link angles ψ_2 and ψ_3 are always 0° , and the maximum of the eight link angles is 39° . In obs2, the eight link angles are all changed due to the obstacle being close to the X_0 axis, and some link angles reached 42° to achieve obstacle avoidance. In obs3, as the position of the obstacle is in the middle and has little influence on the motion of the manipulator, only x_0 and ψ_1 and only ψ_4 – ψ_6 change, with a maximum of 30° . In the absence of obstacles, only x_0 and ψ_1 change, the maximum value of ψ_1 is 32° , and the range of the change in x_0 is smaller than that when obstacles are present.

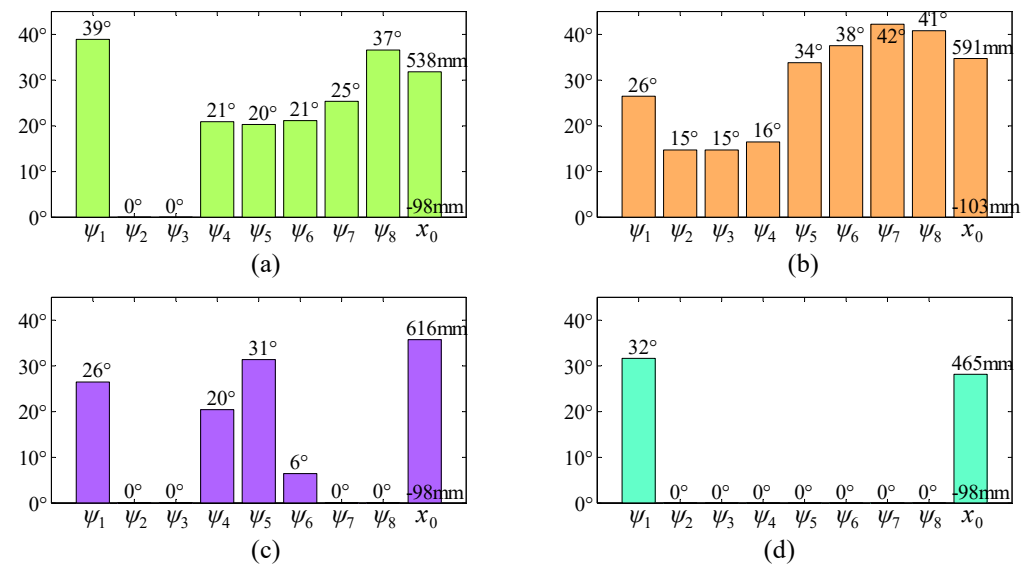


Figure 16. Histogram of the corresponding variation ranges of ψ_i and x_0 in four environments. (a) The range of ψ_i and x_0 in obs1; (b) The range of ψ_i and x_0 in obs2; (c) The range of ψ_i and x_0 in obs3; (d) The range of ψ_i and x_0 without obstacles.

In Section 6.2, the concrete values of ψ_i and x_0 and their corresponding variation laws can be obtained, and the pitch angle θ_i and yaw angle α_i can also be solved. By substituting the solved θ_i and α_i into the forward kinematics, the coordinates and paths of the corresponding end-effector and the center points of each joint can be obtained. The solutions are identical to the expected coordinates and paths, verifying the correctness of the VDSM.

By analyzing the variation rules of the link angle, it can be seen that, when applying VDSM for path planning and solving inverse kinematics, the link angles change as little as possible to achieve the motion of the end-effector along the expected path, which proves that the VDSM has high efficiency.

6.3. Distance between Manipulator and Obstacle

The distances between points (x, y, z) and the axes of obs1, obs2, and obs3, as d_{obs1} , d_{obs2} , and d_{obs3} , respectively, can be calculated by the following equations:

$$d_{\text{obs1}} = \sqrt{(x - 700)^2 + (y - 600)^2}, \quad (22)$$

$$d_{\text{obs2}} = \sqrt{(x - 400)^2 + (y - 400)^2}, \quad (23)$$

$$d_{\text{obs3}} = \sqrt{(y - 2126)^2 + (z - 600)^2}, \quad (24)$$

The line segment is formed between the center points of each two adjacent joints; then, the nearest distance between the line segment and the obstacle is analyzed. Eight groups are analyzed and the minimum value is selected as the distance between the axis of the manipulator and the axis of the obstacle. Thus, the diagram of the distance between the manipulator and the obstacle, as shown in Figure 17, can be obtained.

It can be observed that, because the distance between the surface and the axis of the obstacle is 200 mm from Figure 17. The distance between the manipulator and obstacle is always greater than 265 mm. The distance between the surface of the manipulator and the axis of the obstacle is 61.5 mm. Collision with the obstacles will never happen when the HRM moves along the planned path, as 265 mm is always greater than 261.5 mm, which proves that the final planned path complies with the requirements of obstacle avoidance.

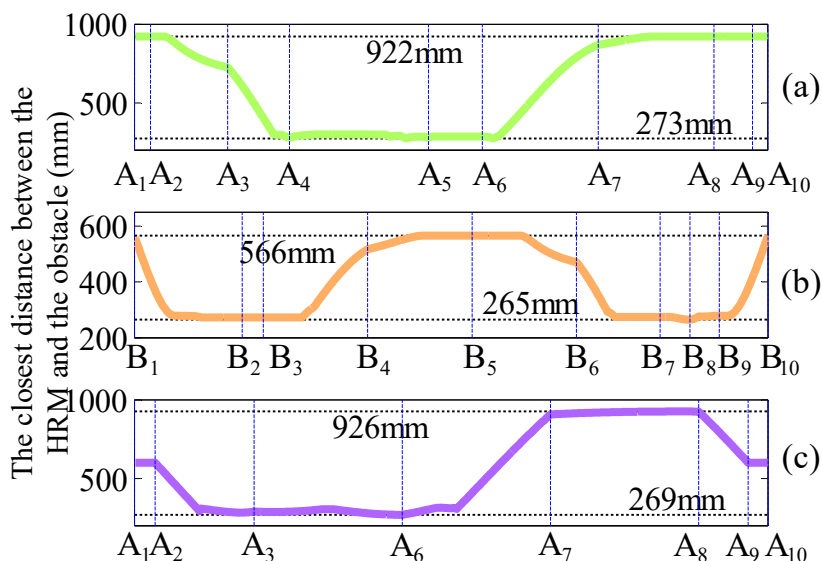


Figure 17. Schematic diagram of the distance between the manipulator and obstacle. (a) The distance between manipulator and obstacle in obs1; (b) The distance between manipulator and obstacle in obs2; (c) The distance between manipulator and obstacle in obs3.

6.4. Change Rules of Driving Cable Length

The coordinates of the center points of each joint can be obtained through simulation. Afterward, the angles of each joint are calculated through inverse kinematics, and then the length of the driving cable can be determined. In this section, an example, as shown in Figure 18, is used to verify the correctness of the inverse kinematics solution. The figure shows the changes in the lengths of 24 driving cables at the first joint when the manipulator is at different positions in obs1. During the process of the manipulator moving from A5 to A6, ψ_1 barely changes, resulting in approximate invariants of the 24 curves in Figure 18. The forward kinematics of these cables' lengths are solved, and the obtained pitch angle θ_i and yaw angle α_i are identical to the simulation results, which verifies the correctness of the proposed method.

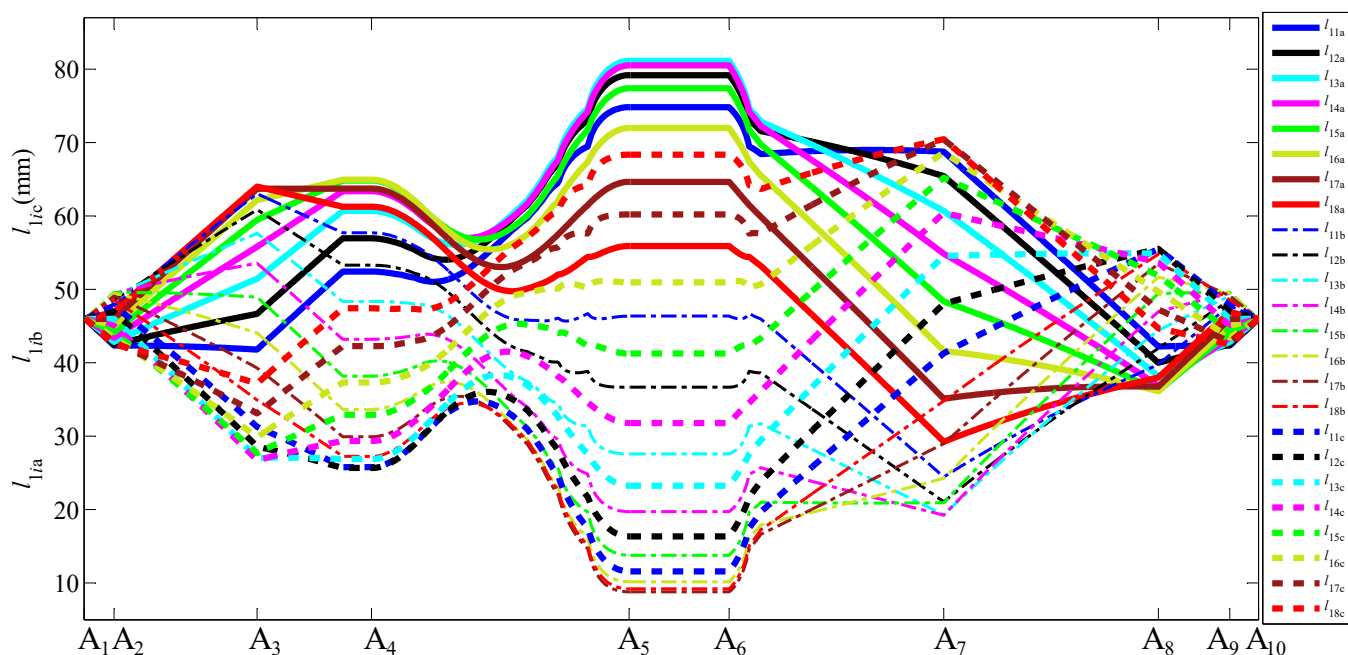


Figure 18. Length change curve of the 24 driving cables at the first joint in obs1.

7. Experiments

The path drawn by the VSDM is a non-repeated path, and the dynamic picture of the manipulator moving along the path can be generated by the simulation software, verifying the VSDM. In this section, for the third obstacle, VSDM is used to plan the path, and the feasibility of the algorithm is verified by experiments. In order to improve the accuracy and robustness of the manipulator operation, a basic PID closed-loop control system is designed, and the corresponding experiments are carried out to obtain the motion diagram of the HRM, as shown in Figure 19. It can be seen from the figure that the HRM can not only avoid obstacles, but also achieve the purpose of moving the end along the square path.

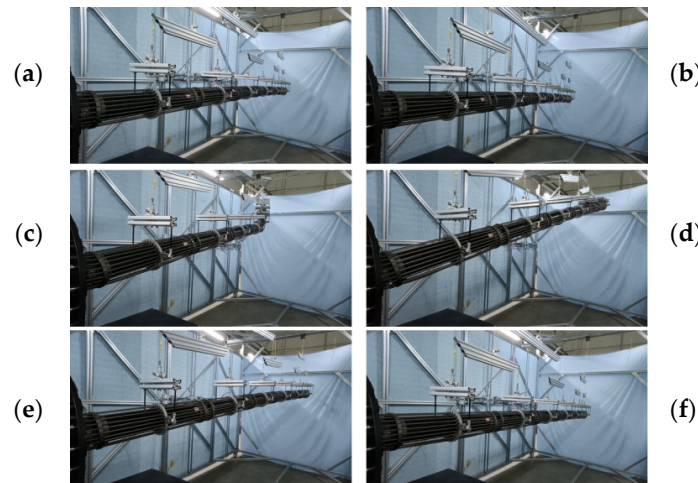


Figure 19. Physical image of the movement process of the HRM. (a) First scenario; (b) Second scenario; (c) Third scenario; (d) Fourth scenario; (e) Fifth scenario; (f) Sixth scenario.

The actual change curve of the joint angle, as shown in Figure 20, can be obtained through experimentation, which is very close to the theoretical change curve of the joint angle obtained through simulation. According to the difference between the theoretical value and the actual value, the error curve of the joint angle shown in Figure 21 can be obtained. Figures 20 and 21 contain the change curves of the actual values and error of 16 joint angles, and the error curve of each joint angle includes two dashed lines of $\pm 0.3^\circ$ to show the main range of the error change.

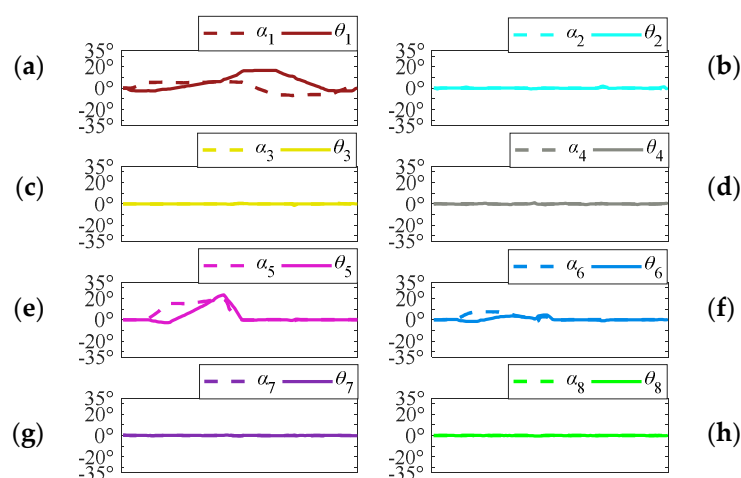


Figure 20. Diagram of the actual changes in joint angles in the non-repeating path experiment. (a) Angular change curve at 1st joint; (b) Angular change curve at 2nd joint; (c) Angular change curve at 3rd joint; (d) Angular change curve at 4th joint; (e) Angular change curve at 5th joint; (f) Angular change curve at 6th joint; (g) Angular change curve at 7th joint; (h) Angular change curve at 8th joint.

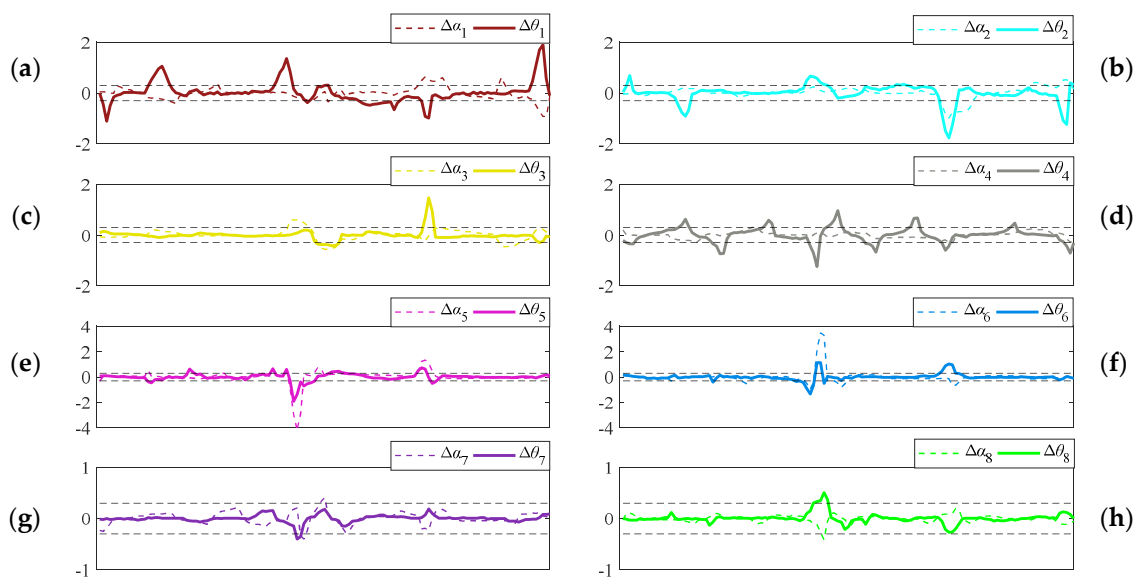


Figure 21. Diagram of the error values of the joint angles in the non-repeating path experiment. (a) Angular error change curve at 1st joint; (b) Angular error change curve at 2nd joint; (c) Angular error change curve at 3rd joint; (d) Angular error change curve at 4th joint; (e) Angular error change curve at 5th joint; (f) Angular error change curve at 6th joint; (g) Angular error change curve at 7th joint; (h) Angular error change curve at 8th joint.

From Figures 20 and 21, it can be seen that the error is small, the joint angle is always within 35° , and the link angle is always within the specified range, which verifies the VDSM corresponding to this experiment. At the same time, it can be verified that, by adopting this method, the end point can move along the desired path while avoiding obstacles with as few changes in the degrees of freedom as possible. In this experiment, only 6 rotational degrees of freedom are changed, and the expected value of the other 10 rotational degrees of freedom is always 0° . The only drawback is that there is external interference in the experiment, which results in a large joint angle error in some places. For example, the errors of α_5 and α_6 are about 4° under the effect of interference, but the error quickly changes to less than 0.3° according to the regulation function of the closed-loop system. In conclusion, the actual value of the angle is always within the specified range, and diverse tasks are achieved, which verifies the effectiveness of the VDSM.

Through simulation and experimental verification, it can be concluded that the VDSM has the following main advantages. The method can change the number of link angles as little as possible in the process of achieving the movement of the end-effector along the desired path. The method makes full use of the redundant properties of HRMs and can achieve obstacle avoidance. The method is suitable for all kinds of obstacles.

8. Conclusions

In this paper, the variable dimensional scaling method (VDSM) is proposed to solve the non-uniqueness and complexity of the inverse kinematics solution of a hyper-redundant manipulator (HRM) and make the end-effector follow the expected path when obstacle avoidance is considered. In this method, the path of the end-effector is scaled according to a certain proportion, and the path of the end-effector and center point of each joint are adjusted according to the specific position of the obstacle, affording the method good versatility. The simulation and experiment were carried out in an environment without obstacles and three environments with different obstacles. It was proven that the VDSM was effective in adjusting the path of each joint center by analyzing the planned motion path, and a certain proportional relationship about the 2D projection plane of the path of each joint center was also proved. Additionally, it was proven that the least change in the link angle was introduced to realize the motion of the end-effector along the desired path

when the change was not more than 42° during the process of the motion by analyzing the variation law of the link angle in the method.

In the future, the proportional relationship between the path sizes of each joint can be variable. The zoom center point can be selected at places other than point $Y = 0$ and $Z = 0$. Dynamic obstacle avoidance can be analyzed based on the VDSM. In this paper, the 3D path was projected onto a plane, and the 3D path can be projected onto a parameter-controlled curved surface to analyze whether the solution of inverse kinematics was optimized.

Author Contributions: Conceptualization, L.J. and Y.H.; methodology, L.J. and Z.Y.; software, L.J. and H.Z.; validation, Z.P., Y.O., and Y.G.; formal analysis, Y.O.; investigation, Z.P.; resources, Z.P.; data curation, L.J.; writing—original draft preparation, L.J. and Y.G.; writing—review and editing, Y.H. and Y.G.; visualization, H.Z.; supervision, Z.Y.; project administration, Y.H.; funding acquisition, Y.H. All authors have read and agreed to the published version of the manuscript.

Funding: This research received no external funding.

Data Availability Statement: Not applicable.

Conflicts of Interest: The authors declare no conflict of interest.

References

- Xu, Q.; Zhan, Q. A real-time inverse kinematics solution based on joint perturbation for redundant manipulators. *Mech. Sci.* **2021**, *12*, 221–235. [\[CrossRef\]](#)
- Wang, X.; Liu, X.; Chen, L.; Hu, H. Deep-learning damped least squares method for inverse kinematics of redundant robots. *Measurement* **2021**, *171*, 108821. [\[CrossRef\]](#)
- Safeea, M.; Bearee, R.; Neto, P. A modified DLS scheme with controlled cyclic solution for inverse kinematics in redundant robots. *IEEE Trans. Ind. Inform.* **2021**, *17*, 8014–8023. [\[CrossRef\]](#)
- Zhang, X.; Fan, B.; Wang, C.; Cheng, X. An improved weighted gradient projection method for inverse kinematics of redundant surgical manipulators. *Sensors* **2021**, *21*, 7362. [\[CrossRef\]](#) [\[PubMed\]](#)
- Xie, Z.; Jin, L.; Luo, X.; Sun, Z.; Liu, M. RNN for repetitive motion generation of redundant robot manipulators: An orthogonal projection-based scheme. *IEEE Trans. Neural Netw. Learn. Syst.* **2022**, *33*, 615–628. [\[CrossRef\]](#) [\[PubMed\]](#)
- Xu, Z.; Li, S.; Zhou, X.; Yan, W.; Cheng, T.; Huang, D. Dynamic neural networks based kinematic control for redundant manipulators with model uncertainties. *Neurocomputing* **2019**, *329*, 255–266. [\[CrossRef\]](#)
- Hideaki, T.; Nozomu, A.; Takao, S.; Yasuo, K. Neural network-based construction of inverse kinematics model for serial redundant manipulators. *Artif. Life Robot.* **2019**, *24*, 487–493.
- Kramar, V.; Kramar, O.; Kabanov, A. An artificial neural network approach for solving inverse kinematics problem for an anthropomorphic manipulator of robot SAR-401. *Machines* **2022**, *10*, 241. [\[CrossRef\]](#)
- Chen, L.; Ma, Y.; Zhang, Y.; Liu, J. Obstacle avoidance and multitarget tracking of a super redundant modular manipulator based on bezier curve and particle swarm optimization. *Chin. J. Mech. Eng.* **2020**, *33*, 71. [\[CrossRef\]](#)
- Serkan, D.; Raşit, K. Strengthening the PSO algorithm with a new technique inspired by the golf game and solving the complex engineering problem. *Complex Intell. Syst.* **2021**, *7*, 1515–1526.
- Ren, Z.; Wang, Z.; Sun, L. A hybrid biogeography-based optimization method for the inverse kinematics problem of an 8-DOF redundant humanoid manipulator. *Front. Inf. Technol. Electron. Eng.* **2015**, *16*, 607–616. [\[CrossRef\]](#)
- Zhang, Q.; Wang, D.; Gao, L. Research on the inverse kinematics of manipulator using an improved self-adaptive mutation differential evolution algorithm. *Int. J. Adv. Robot. Syst.* **2021**, *18*, 17298814211014413. [\[CrossRef\]](#)
- Marcos, M.; Machado, J.; Azevedo, P. A multi-objective approach for the motion planning of redundant manipulators. *Appl. Soft Comput.* **2012**, *12*, 589–599. [\[CrossRef\]](#)
- Claudio, U.; Daniel, S. Design and implementation of a graphic simulator for calculating the inverse kinematics of a redundant planar manipulator robot. *Appl. Sci.* **2020**, *10*, 6770.
- Serkan, D.; Raşit, K. Calculation of the inverse kinematics solution of the 7-DOF redundant robot manipulator by the firefly algorithm and statistical analysis of the results in terms of speed and accuracy. *Inverse Probl. Sci. Eng.* **2020**, *28*, 601–613.
- Dereli, S.; Koker, R. A meta-heuristic proposal for inverse kinematics solution of 7-DOF serial robotic manipulator: Quantum behaved particle swarm algorithm. *Artif. Intell. Rev.* **2020**, *53*, 949–964. [\[CrossRef\]](#)
- Hsu, H. Printed circuit board assembly planning for multi-head gantry SMT machine using multi-swarm and discrete firefly algorithm. *IEEE Access* **2021**, *9*, 1642–1654. [\[CrossRef\]](#)
- Dereli, S.; Koker, R. Simulation based calculation of the inverse kinematics solution of 7-DOF robot manipulator using artificial bee colony algorithm. *SN Appl. Sci.* **2020**, *2*, 27. [\[CrossRef\]](#)
- Colucci, G.; Botta, A.; Tagliavini, L.; Cavallone, P.; Baglieri, L.; Quaglia, G. Kinematic modeling and motion planning of the mobile manipulator Agri.Q for precision agriculture. *Machines* **2022**, *10*, 321. [\[CrossRef\]](#)
- Lee, C.; An, D. AI-based posture control algorithm for a 7-DOF robot manipulator. *Machines* **2022**, *10*, 651. [\[CrossRef\]](#)

21. Huang, Y.; Jia, L.; Chen, J.; Zheng, J.; Guo, Y.; Tao, Y. A novel path planning algorithm considering the maximum deflection angle of joint. *IEEE Access* **2021**, *9*, 115777–115787. [[CrossRef](#)]
22. Xie, H.; Wang, C.; Li, S.; Hu, L.; Yang, H. A geometric approach for follow-the-leader motion of serpentine manipulator. *Int. J. Adv. Robot. Syst.* **2019**, *16*, 1729881419874638. [[CrossRef](#)]
23. Jia, L.; Huang, Y.; Chen, T.; Guo, Y.; Yin, Y.; Chen, J. MDA+RRT: A general approach for resolving the problem of angle constraint for hyper-redundant manipulator. *Expert Syst. Appl.* **2022**, *193*, 116379. [[CrossRef](#)]
24. Zhang, X.; Liu, J.; Ju, Z.; Yang, C. Head-raising of snake robots based on a predefined spiral curve method. *Appl. Sci.* **2018**, *8*, 2011. [[CrossRef](#)]
25. Rodríguez-Molina, A.; Solís-Romero, J.; Villarreal-Cervantes, M.; Serrano-Pérez, O.; Flores-Caballero, G. Path-planning for mobile robots using a novel variable-length differential evolution variant. *Mathematics* **2021**, *9*, 357. [[CrossRef](#)]